

# A method to quantify the advantages of a variable valve train for CI engines

Giordano Moretto<sup>1</sup> , Severin Hänggi<sup>1</sup> , Andyn Omanovic<sup>2</sup>,  
Alois Amstutz<sup>1</sup> and Christopher Onder<sup>1</sup>

International J of Engine Research

2024, Vol. 25(1) 3–23

© IMechE 2023



Article reuse guidelines:

sagepub.com/journals-permissions

DOI: 10.1177/14680874231204113

journals.sagepub.com/home/ijer



## Abstract

Today's CI engines are subject to strict regulations of pollutant emissions and ambitious fuel consumption targets. Therefore, the interaction between the engine and the exhaust aftertreatment system (ATS) has become increasingly important. Numerous studies have shown that a variable valve train (VVT) improves the interaction between engine and ATS. However, most of these studies either quantify the advantage on a specific engine or only present complex CFD models, such that the results are not easily transferable to different engines. Thus, engine manufacturers cannot directly use these results to assess the advantage of various VVT strategies for their engines. In this paper, we propose a cycle-discrete cylinder model based on first principles which allows to simulate various VVT strategies. In contrast to present methods based on CFD, the proposed cylinder model can be realized with the equations presented. Furthermore, the model is identified with measurement data of an engine without a VVT. A separate engine, which is retrofitted with a fully VVT, is used to validate the proposed modeling approach. Using the identified model in combination with a mean-value model of the air path, we are able to simulate the effects of early intake valve closing, early exhaust valve opening, and cylinder deactivation for a complete CI engine that has no VVT installed. The model is then used to highlight the advantage of a VVT for two scenarios at part-load operation. At cold start, where the temperature of the ATS must be increased quickly, variable valve timing achieves higher enthalpy flows to the ATS while also lowering engine-out NO<sub>x</sub> emissions when compared to a standard engine strategy. If the ATS is at the operating temperature, cylinder deactivation achieves significantly higher enthalpy flows which prevents the ATS from cooling down. In addition, cylinder deactivation also lowers fuel consumption and engine-out NO<sub>x</sub> emissions.

## Keywords

CI engine, variable valve train, variable valve timing, cylinder model, variable engine calibration, cylinder deactivation

Date received: 22 December 2022; accepted: 20 April 2023

## Introduction

Numerous variable valve train (VVT) systems for CI engines that feature various capabilities in terms of valve timing, valve lift, and actuation speed are presented in literature. Since most of the advantages are achieved by using variable valve timing and cylinder deactivation, we will limit our review to this specific case. The resulting effects are based on steady-state engine results and can be categorized into three categories. First, by adapting the valve timings for each engine speed, a VVT optimizes the cylinder gas exchange with the air path. This can be used to increase low-speed engine torque or to further increase efficiency for various engine speeds.<sup>1–3</sup> In addition, a VVT can also be used for engine braking.<sup>1,4</sup> Second, numerous authors assess the trade-off between engine efficiency and engine-out emissions. The most prominent

example is the use of early intake valve closing (IVC), which improves engine brake efficiency due to reduced pumping loss.<sup>5–8</sup> The early IVC strategy is also known as Miller cycle. If the boost pressure is not increased, early IVC results in higher soot emissions due to a decrease in engine mass flow. In combination with a highly efficient turbo-charging system and increased boost pressure, the Miller cycle improves efficiency

<sup>1</sup>Institute for Dynamic Systems and Control, ETH Zürich, Zurich, Switzerland

<sup>2</sup>Automotive Powertrain Technologies Laboratory, Empa Dübendorf, Dübendorf, Switzerland

### Corresponding author:

Giordano Moretto, Institute for Dynamic Systems and Control, ETH Zurich, Sonneggstrasse 3, Zurich 8092, Switzerland.

Email: morettog@idsc.mavt.ethz.ch

over a wide load range without increasing soot emissions.<sup>9,10</sup> In addition, the Miller cycle also lowers engine-out NOx emissions,<sup>2,5,9,11</sup> which positively affect the inherent efficiency-NOx trade-off of CI engines. Third, more recent publications focus on the interaction of a CI engine with a VVT and its exhaust after-treatment system (ATS). In today's CI engines, the ATS plays a key role in the reduction of pollutant emissions. With regard to NOx emissions, SCR catalysts only work if the catalyst is operated in a narrow temperature window of 250 – 400°C.<sup>12</sup> This becomes an issue at cold start, where the temperature is too low, as well as at part-load operation, where the catalyst temperature might drop below the light-off temperature. In both cases, which are known as warm-up operation and stay-warm operation, the engine must provide enthalpy to the ATS. Since the overall goal is to achieve the lowest possible fuel consumption over a pre-defined cycle while still being compliant with tail-pipe NOx emission limits, the complete system of engine and ATS must be optimized. Recent studies have proposed a framework to jointly optimize the engine and ATS for transient operation using a variable engine calibration.<sup>13–16</sup> This framework allows to operate the engine at the Pareto-optimal trade-off curves of efficiency, NOx emissions, and exhaust enthalpy. The latter quantity is used to ensure that the ATS is operated in the correct temperature window. A variety of strategies are used in regard to variable valve timing: Miller cycle, early exhaust valve opening (EVO), and increased internal EGR, or various combinations thereof. The latter strategy is achieved either by early exhaust valve closing (EVC) and therefore an increased negative valve overlap or by late EVC or reopening of the exhaust valve that results in the rebreathing of exhaust gas from the exhaust manifold. Most of the strategies mentioned increase the engine-out enthalpy at the expense of increased fuel consumption.<sup>3,6,7,17–23</sup> Alternatively, various cylinder deactivation strategies can also be used to increase exhaust enthalpy.<sup>7,8,24–28</sup> In comparison to the valve timing strategies mentioned, cylinder deactivation results in a higher engine-out temperature, but it also lowers engine mass flow and is therefore better suited for stay-warm operation.<sup>24</sup> Several authors have already demonstrated that VVT strategies offer advantages for the complete engine system during various transient cycles.<sup>19,20,24,25</sup> However, to the best of our knowledge no author has compared early IVC, early EVO, and cylinder deactivation simultaneously. The advantages mentioned above focus on CI engines with conventional heterogeneous combustion only. Variable valve trains are increasingly being investigated for novel engine concepts. For CI engines, those investigations mostly feature the combustion concepts premixed charge compression ignition (PCCI) and reactivity controlled compression ignition (RCCI). By controlling the cylinder charge composition and effective compression ratio, a VVT improves and extends the operation

of PCCI engines.<sup>29–34</sup> Similar advantages have been shown for RCCI engines.<sup>35–38</sup> For the analysis below, we will limit our focus on the advantages of using a VVT on conventional CI engines.

To the best of the authors' knowledge no simple methodology exists that allows to quantify the advantages of including a VVT on an existing engine layout. Most experimental publications<sup>2,3,6,7,17,20–22,24–28</sup> assess the advantages gained on a specific engine, which are not directly transferable to other engines. Other publications<sup>2,5,11,19</sup> use complex CFD simulation tools that require proprietary software and in-depth knowledge of fluid dynamics. Hence, engine manufacturers cannot easily assess if the advantages to be gained by retrofitting their current engine with a VVT is worth the increased effort. In addition, the results are often not discussed for the complete engine system which also features the air path and ATS. If no ATS is directly included in the analysis, the results must be discussed in the context of the triple trade-off of efficiency, NOx emissions, and exhaust enthalpy.

Our contribution is threefold: First, we propose a cycle-discrete model based on first principles that describes the charge, combustion, and discharge of an engine cylinder with negative valve overlap. We integrate the cylinder model into an existing air path model<sup>39</sup> to simulate the complete engine as a mean-value model. Second, the model proposed is able to simulate various VVT strategies, such as early IVC (Miller cycle), early EVO, and cylinder deactivation. We assume a VVT system that can change valve timing and cylinder deactivation on a cycle-to-cycle basis. The model is identified with standard valve timing only and allows for the extrapolation of the VVT strategies mentioned. In contrast to existing approaches, the cylinder models proposed can be implemented using the presented equations without the need of any additional simulation tools. The models proposed, which are used for the simulation of various VVT strategies, have been validated on a separate engine retrofitted with a fully variable valve train. Figure 1 shows an overview of the method proposed. Finally, we demonstrate the advantages of various VVT strategies for a CI engine at part-load and steady-state operation. The presented case study demonstrates how optimal solutions are obtained systematically by studying the Pareto-optimal trade-off curves for fuel consumption, engine-out NOx emissions, and enthalpy provided to the ATS. We thereby show that the cylinder models proposed can be used to easily quantify the benefits of various VVT-strategies.

This paper is structured as follows: Section 2 introduces the experimental setup. In Section 3 the discrete-event cylinder model is presented together with the model extensions that allow for the simulation of early IVC, early EVO, and cylinder deactivation. Section 4 then shows the cylinder model identified and the validation of the model extensions proposed on a separate engine retrofitted with a VVT. Finally, Section 5 shows a simulative case study for a CI engine with a VVT and

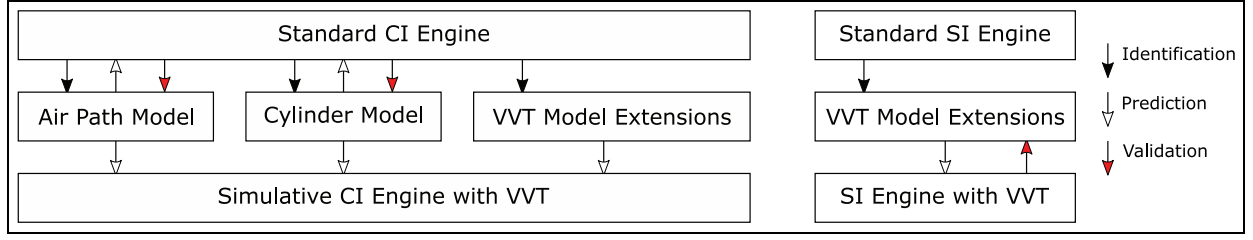


**Figure 1.** An overview of the proposed method. We use measurements of a CI engine without a VVT to create a simulative model of the same engine with various VVT capabilities. The proposed identification of the VVT model extensions are validated on an engine which has been retrofitted with a VVT.

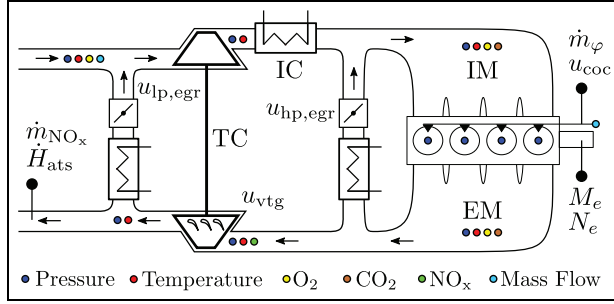


**Figure 2.** Layout of engine A. Only the most relevant sensors are shown.

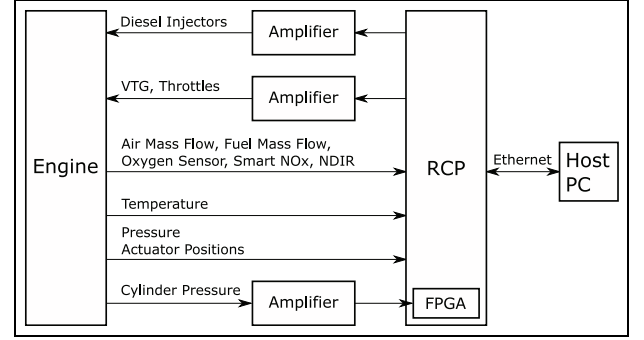


**Figure 3.** Testbench setup for engine A.

the improvements which result in terms of Pareto-optimal solutions of fuel consumption, engine-out NO<sub>x</sub> emissions, and exhaust enthalpy.

## Experimental setup

The engine of interest, which has no VVT installed, is a Volkswagen Diesel engine of the EA189 engine-family. The engine system includes a turbocharger (TC) with a variable turbine geometry (VTG), a high-pressure EGR path (HP EGR), and a common-rail injection system. Furthermore, the engine is retrofitted with a low-pressure EGR path (LP EGR). Figure 2 shows an overview of the engine, which will be denoted as engine A. The engine operating point is defined by the engine torque  $M_e$  and the engine speed  $N_e$ . The outputs of interest are: the fuel mass flow  $\dot{m}_\phi$ , the mass flow of NO<sub>x</sub>  $\dot{m}_{NO_x}$  to the ATS, and the enthalpy to the ATS  $\dot{H}_{ats}$  defined as

$$\dot{H}_{ats} = c_{p, eg} \cdot \dot{m}_{ats} \cdot (T_{at} - T_{ats}), \quad (1)$$

where  $T_{ats}$  denotes the temperature of the ATS and  $T_{at}$  the temperature after turbine. In order to maximize  $\dot{H}_{ats}$ , we can either vary  $\dot{m}_{ats}$  or  $T_{at}$ , while  $T_{ats}$  is set. The intercooler after the compressor allows to control the temperature of the fresh charge in the intake manifold. The engine has numerous sensors in the intake manifold (IM), the exhaust manifold (EM), and in other locations. In addition, each cylinder is equipped with a cylinder pressure sensor.

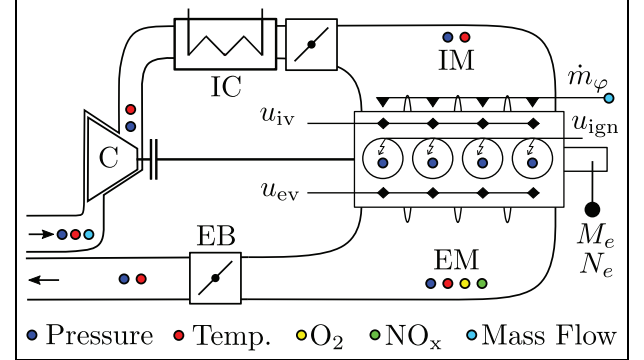


**Figure 4.** Layout of engine B. The exhaust brake (EB) can be used to increase the exhaust manifold pressure which is used to simulate the back pressure caused by a turbocharger.

Figure 3 shows a detailed overview of the test bench setup for engine A. A rapid control prototyping system (RCP) from dSpace is used to control the engine and record all signals. The engine control software is developed completely in-house. An FPGA-board on the RCP allows for a fast evaluation of the cylinder pressure signals, which can be used for a cycle-to-cycle control of the fuel injection. The oxygen concentration is measured with standard wide-band lambda-sensors, whereas NO<sub>x</sub> is measured with a smart NO<sub>x</sub> lambda-sensor. To measure the CO<sub>2</sub> concentration, we use NDIR-sensors. Both air and fuel mass flow are measured with ultrasonic-based sensors. A second engine called engine B, which is retrofitted with a VVT system, is used for validation of the proposed model extensions. Figure 4 shows an overview of this engine. The electro-

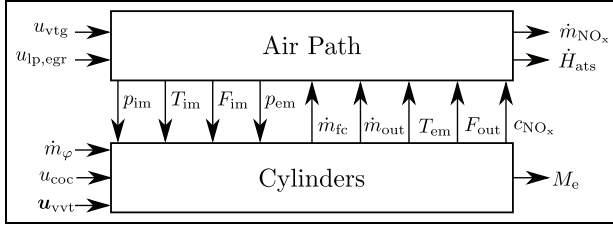


**Figure 5.** The process model consists of the air path model and the cylinder model. The various VVT inputs are summarized by  $u_{vvt}$ . All other variables will be introduced below.

hydraulic valve system allows for a fully variable valve timing and cylinder deactivation on a cycle-to-cycle basis.<sup>40</sup> In addition, the system is easily controlled and shows a high efficiency due to the recuperation of valve motion energy. The spark-ignited engine is of the Volkswagen engine family EA111 and is retrofitted with a port-fuel natural-gas injection. The proposed VVT models, which are validated on this engine, are independent of the type of ignition. The screw compressor is connected to the engine crankshaft and can be decoupled by a clutch. Furthermore, the intercooler can be bypassed (not shown here). The most important specifications for both engines are summarized in Table A1 in Appendix A.2.

## Process model

The process model consists of two parts: the air-path model and the cylinder model. Figure 5 shows an overview of the various inputs and outputs of these models. In this section, we derive a cylinder process model that enables the simulation of the VVT strategies mentioned above. The model is based on first principles and features regression functions which are determined by experiments. We first derive a model with standard valve timing only and then present the extensions to model variable valve timing and cylinder deactivation. The air path is modeled by an existing mean-value model which has already been validated.<sup>39</sup> Other forms of air-path models can be used as long as the interactions to the cylinder model remain unchanged. For the layout of engine A, previous analyses showed no advantages for a steady-state optimization of HP EGR when compared to LP EGR.<sup>39</sup> Therefore, HP EGR is neglected in the analysis below.

### Basic definitions

The Willans approximation links the brake mean effective pressure  $p_{me}$  and the injected fuel mean effective pressure  $p_{m\phi}$  by the linear affine relation

$$p_{me} = e \cdot p_{m\phi} + p_{me0}. \quad (2)$$

The term  $e$  represents the thermodynamic efficiency of the combustion, whereas the fuel mean effective pressure is defined as

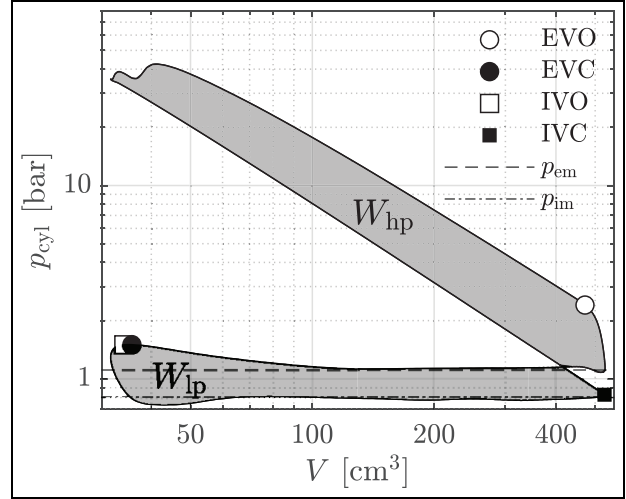


**Figure 6.** Exemplary  $p$ - $V$  diagram of engine A.

$$p_{m\phi} = \frac{h_{lv} \cdot m_{\phi}}{V_d}, \quad (3)$$

where  $h_{lv}$  represents the lower heating value and  $V_d$  the displacement volume of a single cylinder. The injected fuel mass for a single cylinder per cycle is obtained by

$$m_{\phi} = \dot{m}_{\phi} \cdot \frac{4 \cdot \pi}{\omega_e \cdot n_{cyl}}, \quad (4)$$

where  $\omega_e$  represents the engine angular velocity and  $n_{cyl}$  the number of cylinders. The affine term of equation (2) can be rewritten as

$$p_{me0} = p_{me0f} + p_{me0g}, \quad (5)$$

where  $p_{me0g}$  represents the pumping loss and  $p_{me0f}$  the friction loss, respectively. The quantities of the Willans approximation can be derived from the cylinder pressure signal. Figure 6 shows a generic  $p$ - $V$  diagram of a 4-stroke engine which is used to obtain

$$e = \frac{W_{hp}}{m_{\phi} \cdot h_{lv}}, \quad (6)$$

$$p_{me0g} = \frac{W_{lp}}{V_d},$$

where  $W_{hp}$  denotes the high-pressure indicated work and  $W_{lp}$  the low-pressure indicated work, also known as pumping loss. It is largely defined by the pressure difference over the engine

$$\Delta p_{eng} = p_{em} - p_{im}. \quad (7)$$

In the text below, the term “pumping loss” will be used interchangeably for  $W_{lp}$  and  $p_{me0g}$ .

Figure 7 shows the proposed valve-area model. The effective valve area  $A_{eff}$  is assumed to have a trapezoidal shape.<sup>41</sup> The changes from the standard valve timings are defined as

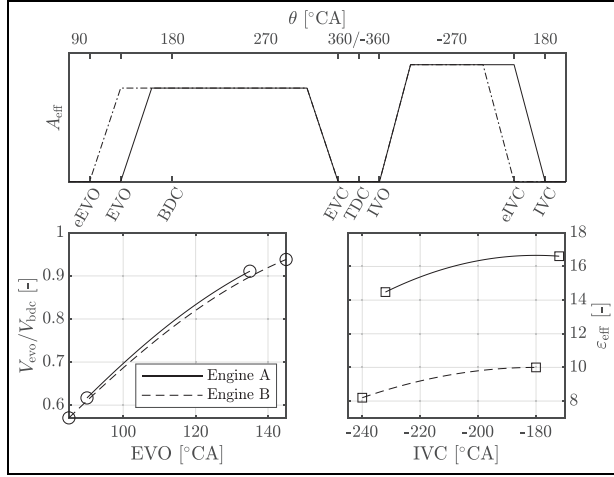


**Figure 7.** The top plot shows the effective valve areas for intake valve and exhaust valve with respect to valve timing. No valve overlap is considered. The bottom plots show the range of valve timings investigated for each engine, respectively.

$$\begin{aligned}\Delta u_{ivc} &= u_{ivc,0} - u_{ivc}, \\ \Delta u_{evo} &= u_{evo,0} - u_{evo}\end{aligned}\quad (8)$$

and are assumed not to change the overall shape of  $A_{eff}$ . For the further derivations, we must introduce a few definitions. The effective compression ratio is defined as

$$\epsilon_{eff} = \frac{V_{ivc}}{V_c}, \quad (9)$$

where  $V_c$  represents the clearance volume of the cylinder at top dead center (TDC) and  $V_{ivc}$  the volume at IVC.

### Cylinder model

The cylinder is represented by a discrete-event model, which is based on the cycle-to-cycle dynamics of the residual cylinder charge at EVC. The discrete model itself is divided into different stages which track the evolution of the cylinder states

$$\mathbf{x} := [m, T, F]^T, \quad (10)$$

where  $m$  denotes the mass,  $T$  denotes the temperature, and  $F$  denotes the oxygen mass fraction of the gas defined as

$$F := \frac{m_{O_2}}{m}. \quad (11)$$

The following notation is used for the discrete-event cycle  $k$ :

$$\mathbf{x}^k := \mathbf{x}(k), \quad (12)$$

whereas the subscripts describe a stage of the cylinder model, for example, for EVC:

$$\mathbf{x}_{evc} = [m_{evc}, T_{evc}, F_{evc}]^T. \quad (13)$$

The cylinder model thus reads as follows:

$$\begin{aligned}\mathbf{x}_{evc}^{k+1} &= \mathbf{f}(\mathbf{x}_{evc}^k, \mathbf{u}^k), \\ \mathbf{y}^k &= \mathbf{g}(\mathbf{x}_{evc}^k, \mathbf{u}^k),\end{aligned}\quad (14)$$

where the states of the discrete-event model are the cylinder states at EVC at cycle  $k$ .

The input to the process model is defined as

$$\mathbf{u} := [m_\phi, u_{coc}]^T, \quad (15)$$

which consists of the injected fuel mass per cylinder per cycle  $m_\phi$  and the center of combustion  $u_{coc}$ . A pre-injection is used to mitigate excess combustion noise.<sup>42</sup> The center of combustion is controlled by a low-level controller. The inputs of the VVT are defined as

$$\mathbf{u}_{vvt} := [\Delta u_{ivc}, \Delta u_{evo}, n_{act}]^T, \quad (16)$$

which represents the variable valve timings (8) and the number of active cylinders  $n_{act}$ . In a first derivation of the cylinder model, the inputs  $\mathbf{u}_{vvt}$  are not considered. An important quantity for each cylinder is the fuel-air equivalence ratio, which is defined as

$$\Phi = \frac{m_\phi \cdot \sigma_0}{m_{ivc}} \cdot \frac{F_{air}}{F_{ivc}}. \quad (17)$$

The parameter  $\sigma_0$  represents the mass ratio for a stoichiometric air-fuel mixture, while the second fraction accounts for the burnt gas inside the cylinder, with  $F_{air}$  being the ambient oxygen mass fraction. The reciprocal value of  $\Phi$  is the well-known air-to-fuel ratio. The outputs of all four cylinders are the engine torque  $M_e$ , the engine-out mass  $m_{out}$  per cycle, the engine-out temperature to the exhaust manifold  $T_{em}$ , the engine-out oxygen concentration  $F_{out}$ , and the NOx concentration  $c_{NO_x}$ , which are summarized as

$$\mathbf{y} = [M_e, m_{out}, T_{em}, F_{out}, c_{NO_x}]^T. \quad (18)$$

This model implies that the cylinder outputs  $\mathbf{y}$  are fully determined by the cylinder states  $\mathbf{x}_{bdc}$ , the input  $\mathbf{u}$ , and the current air path states  $p_{im}, T_{im}, F_{im}, p_{em}$ . Figure 8 shows a simplified causality diagram of the discrete-event cylinder model.

The diagram is a simplification of the complete cylinder model and only shows the most important submodels which are affected by the VVT strategies mentioned. The discrete-event model is now derived on the basis of the various stages during an engine cycle which are shown in Figure 9. For the standard model derivation the VVT inputs are omitted. The first stage of the model starts with EVC, which defines the residual gas charge  $\mathbf{x}_{evc}^k$ . At IVO, some of the residual gas expands to the intake manifold and is aspirated back into the cylinder. The aspirated fresh charge from IVO to IVC can be modeled by a volumetric pump<sup>12</sup>

$$m_{fc}^k = \lambda_1 \cdot \frac{p_{im}^k}{R_{air} \cdot T_{im}^k} \cdot (V_{ivc} - V_{ivo}), \quad (19)$$





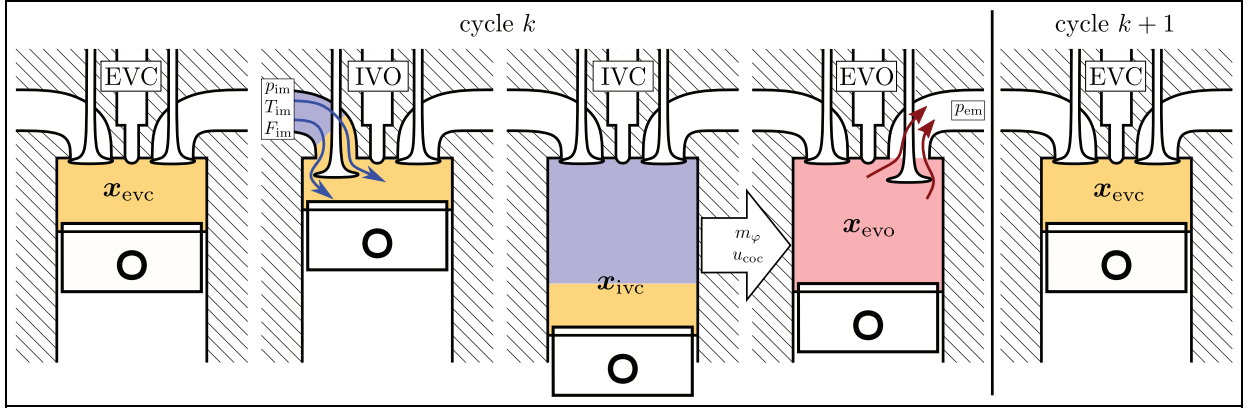


**Figure 9.** Overview of the most important stages of the discrete cylinder model. The states  $\mathbf{x}_{ivc}$  define the states  $\mathbf{x}_{bdc}$  at bottom dead center (BDC). Together with the fuel injection  $\mathbf{u}$ , the states  $\mathbf{x}_{bdc}$  define the states at EVO  $\mathbf{x}_{evo}$ . Together with  $p_{em}$ , the states at EVO define the next cycle. For all stages, we assume a homogeneous mixture.

**Table 1.** Effect of various VVT strategies on the submodels presented above.

Input	Effect	Equation
$\Delta u_{ivc}$	Reduced mass flow	(19) $\dot{m}_{fc}$
	Reduced mass flow	(20) $\lambda_{l,p}$
	Reduced pumping loss	(30) $p_{me0g}$
	Red. compression ratio	(23) $T_{bdc}$
$\Delta u_{evo}$	Work loss	(2) $p_{me}$
	Increased engine-out temp.	(33) $T_{em}$
$n_{act}$	Reduced torque	(2) $p_{me}$
	Reduced mass flow	(34) $\dot{m}_{fc}$
	Reduced mass flow	(4) $\dot{m}_{\phi}$
	Reduced mass flow	(35) $\dot{m}_{out}$

Equations (28) describe the discrete-event state update of equation (14). A detailed derivation is shown in Appendix A.3. The torque  $M_e$  is obtained by means of the Willans approximation of equation (2) for which we need to find expressions for the thermodynamic efficiency

$$e = f_e(\mathbf{x}_{bdc}, \mathbf{u}), \quad (29)$$

and the friction loss and pumping loss

$$\begin{aligned} p_{me0g} &= f_{p_{me0g}}(\Delta p_{eng}), \\ p_{me0f} &= C_{p_{me0f}}. \end{aligned} \quad (30)$$

The engine-out NOx emissions  $c_{NO_x}$  are modeled by

$$c_{NO_x} = f_{c_{NO_x}}(\mathbf{x}_{bdc}, \mathbf{u}), \quad (31)$$

whereas the engine-out mass and oxygen gas mass fraction are obtained by the difference of mass present in the cylinder at EVO and at EVC

$$\begin{aligned} m_{out}^k &= m_{ivc}^k + m_{\phi}^k - m_{evc}^{k+1}, \\ F_{out}^k &= \frac{F_{im}^k \cdot m_{fc}^k + F_{evc}^k \cdot m_{evc}^k - \sigma_{O_2} \cdot m_{\phi}^k}{m_{fc}^k + m_{evc}^k + m_{\phi}^k}. \end{aligned} \quad (32)$$

For the exhaust manifold temperature  $T_{em}$ , two effects have to be considered. First, the exhaust gas that leaves the cylinder loses some of its enthalpy to the exhaust valves, the engine block, and the exhaust manifold. Second, the exhaust gas expands to the exhaust pressure  $p_{em}$ . Hence, if  $p_{em}$  is high,  $T_{em}$  will also be higher. Therefore, we model the exhaust manifold temperature  $T_{em}$  at a reference pressure and then correct it by the current  $p_{em}$ :

$$\begin{aligned} T_{em,ref}^k &= f_{T_{em,ref}}(p_{evo}^k, T_{evo}^k), \\ T_{em}^k &= T_{em,ref}^k \cdot \left( \frac{p_{em}^k}{p_{ref}} \right)^{\frac{\gamma_{eg}-1}{\gamma_{eg}}}. \end{aligned} \quad (33)$$

Finally, we obtain a formulation of the mass flows for use in the mean-value air-path model by the following factor:

$$\dot{m}_{fc} = m_{fc} \cdot \frac{\omega_e \cdot n_{cyl}}{4 \cdot \pi}, \quad (34)$$

$$\dot{m}_{out} = m_{out} \cdot \frac{\omega_e \cdot n_{cyl}}{4 \cdot \pi}. \quad (35)$$

For the model presented, we need to experimentally identify  $f_{p_{evo}}, f_e, f_{p_{me0g}}, f_{c_{NO_x}}, f_{T_{em,ref}}$ , and the constants  $C_{T_{ivc}}, C_{\lambda_1}$ , and  $C_{p_{me0f}}$ .

### Extensions for VVT

The Miller cycle (early IVC), early EVO, and cylinder deactivation are yet to be included in the cylinder model presented. Table 1 shows the effects of these VVT strategies. For the identification of the model, only measurements with standard valve timing are required.

### Miller cycle

The three main effects of the Miller cycle are a reduction in fresh charge, a reduction in pumping loss, and a reduced compression ratio. The effect of an early IVC on the fresh charge is already included in the formulation of equations (19) and (20). Hence, no additional

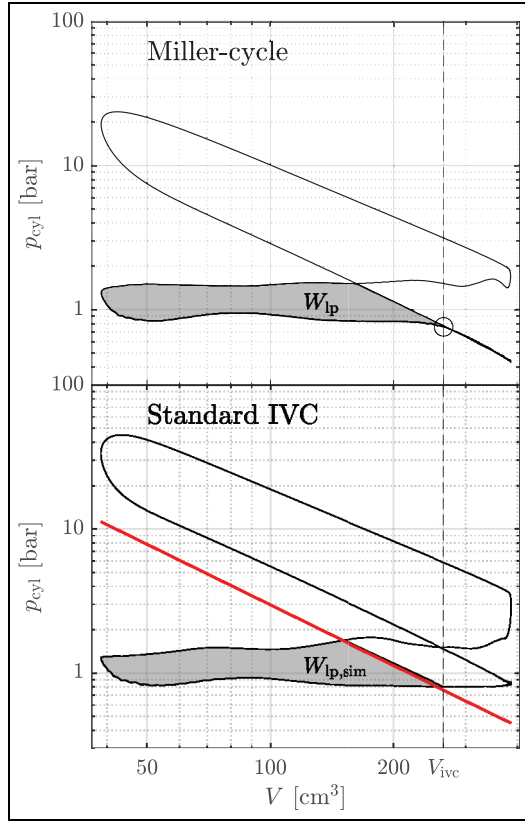


**Figure 10.** The top plot shows the  $p$ - $V$  diagram for a Miller cycle with  $\Delta u_{ivc} = 80^\circ\text{CA}$ , while the bottom plot shows the  $p$ - $V$  diagram for standard IVC. The red line denotes the shifted compression curve of the high-pressure cycle that results in the same  $V_{ivc}$  as for the Miller cycle. Measurements of engine B.

parameters are needed. Figure 10 shows the effect of an early IVC on the gas exchange. The altered pumping loss can be derived from the  $p$ - $V$  diagram with standard IVC by shifting the compression curve to the left until the same IVC occurs as for the  $p$ - $V$  diagram of the Miller cycle. The resulting area to the left of the shifted compression curve represents the simulated reduced pumping loss  $W_{lp,sim}$ . This derivation allows to simulate the quantity  $W_{lp,sim}$  based on standard IVC only. Early IVC also reduces the compression ratio  $\varepsilon_{eff}$ , which ultimately affects the combustion efficiency  $e$ , the NOx emissions  $c_{NO_x}$ , and the engine-out temperature  $T_{em}$ . By assumption, all of these models are completely defined by  $x_{bdc}$ ,  $u$ , and air path states. Since an early IVC causes a drop in  $T_{bdc}$  as shown in equation (23), the effect of a reduced compression ratio is captured in  $x_{bdc}$ . A distinction has to be made for two different types of Miller cycles mentioned in literature. The so-called “unboosted Miller cycle” assumes that an early IVC reduces engine mass flow as described above. In the case of a CI engine with unaltered fuel mass injected this leads to an increase in the fuel-air equivalence ratio  $\Phi$ . On the other hand, the “boosted Miller cycle” assumes that  $\Phi$  remains constant even with an early IVC. For this case, the intake manifold pressure  $p_{im}$  needs to be increased to account for the decreased

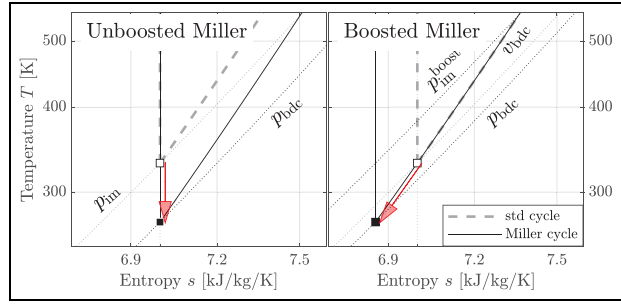


**Figure 11.** Zoomed-in  $T$ - $s$  diagrams for both Miller cycles. The marker “□” denotes  $x_{bdc}$  for standard IVC; the marker “■” denotes  $x_{bdc}$  for early IVC. The red arrows show the shift direction of  $x_{bdc}$ . The unboosted Miller cycle shifts  $x_{bdc}$  along an isentropic line; the boosted Miller cycle shifts  $x_{bdc}$  along an isochoric line  $v_{bdc}$ .

engine mass flow  $m_{fc}$ . Regardless of the type of Miller cycle, either cycle leads to a reduction in  $T_{bdc}$ . Figure 11 shows generic  $T$ - $s$  diagrams for both cycles.

### Early EVO

Two main effects must be modeled for early EVO: a loss of indicated work and an increase in exhaust temperature. Both are caused by the loss of work potential of the expanding gases inside the cylinder. Figure 12 shows two  $p$ - $V$  curves for standard EVO and early EVO.

The work loss compared to standard EVO is calculated by

$$\Delta W = \int_{V_{evo}}^{V_{bdc}} (p_{cyl} - p'_{cyl}) dV, \quad (36)$$

with which we obtain a decrease in load by

$$\begin{aligned} p_{me} &= \frac{W_{hp} - \Delta W}{m_\phi \cdot h_{lhv}} \cdot p_{m\phi} + p_{me0}, \\ &= e \cdot p_{m\phi} + p_{me0} - \frac{\Delta W}{V_d}. \end{aligned} \quad (37)$$

Figure 13 depicts the various control volumes of the exhaust path that are required to derive a model for the increase in temperature. In addition, we need to make the following assumptions for the derivation: an early EVO does not change  $T_{evc}$  and therefore  $\dot{m}_{out}$ ; the cylinder is adiabatic during the discharge process; the control volume “exhaust piping” is in steady-state; all heat losses occur in this control volume and are proportional to the enthalpy leaving the cylinder.

First, we define the enthalpy that enters the exhaust manifold:

$$\dot{H}_{em} = c_{p,eg} \cdot \dot{m}_{out} \cdot T_{em}, \quad (38)$$

where  $\dot{m}_{out}$  and  $T_{em}$  represent mean-value model quantities. Since we assume that the mass flow  $\dot{m}_{out}$  does not change with early EVO, the new enthalpy must read as follows:

$$\dot{H}'_{em} = c_{p,eg} \cdot \dot{m}_{out} \cdot (T_{em} + \Delta T). \quad (39)$$



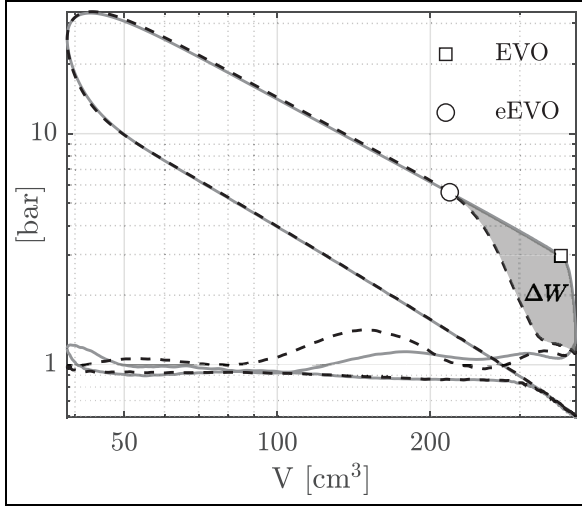


**Figure 12.** The dashed line shows the cylinder pressure  $p'_{cyl}$  due to early EVO, the gray line shows the cylinder pressure  $p_{cyl}$  for standard EVO. The difference between the two pressure curves can be used to calculate the work loss  $\Delta W$ . Data of engine B.

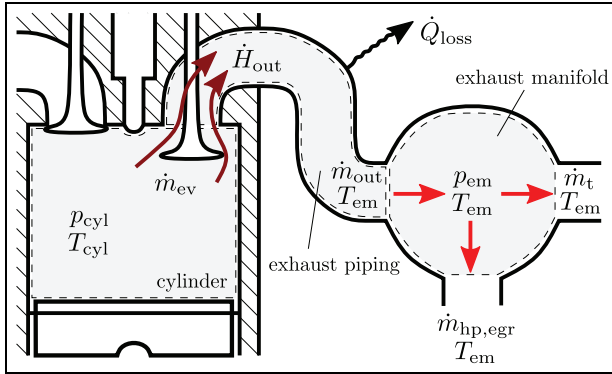


**Figure 13.** Model of the exhaust path used for the derivation of the enthalpy increase due to early EVO. The model uses three different control volumes: cylinder, exhaust piping, and exhaust manifold. The control volumes are indicated by dashed lines.

In order to find an expression for  $\Delta T$ , we first have to correlate the cylinder-out enthalpy flow  $\dot{H}_{out}$  with  $\dot{H}_{em}$ . Using the steady-state assumption for the control volume “exhaust piping” yields the relation

$$\begin{aligned}\dot{H}_{out} &= \dot{Q}_{loss} + \dot{H}_{em}, \\ &= H_{out} \cdot \frac{n_{cyl} \cdot \omega_e}{4 \cdot \pi},\end{aligned}\quad (40)$$

where  $\dot{Q}_{loss}$  accounts for all heat losses of the exhaust gas to the exhaust valve, engine block, and exhaust piping. The quantity  $H_{out}$  is obtained by simulation of a crank-angle-resolved cylinder model and represents the cumulated enthalpy flow out of a single cylinder during the discharge process. A detailed derivation is found in Appendix A.4. By the assumption mentioned above, we obtain that both enthalpy flows are related by

$$\eta_Q := \frac{\dot{H}_{em}}{\dot{H}_{out}}, \quad (41)$$

where  $\eta_Q$  represents the heat transfer efficiency. Once  $\eta_Q$  is determined by experimental data, we can directly relate  $\dot{H}_{out}$  with  $\dot{H}_{em}$ . For the further derivation, we use quantities based on a cycle-to-cycle basis. Since we assume the cylinder to be adiabatic, the complete work loss  $\Delta W$  must be converted to enthalpy leaving the cylinder and hence

$$H'_{out} = H_{out} + \Delta W. \quad (42)$$

Using the above equations for a single cylinder and on a cycle-discrete basis, we conclude that

$$\begin{aligned}\Delta T &= \frac{H'_{em} - H_{em}}{c_{p, eg} \cdot m_{out}}, \\ &= \frac{H'_{em}}{c_{p, eg} \cdot m_{out}} - T_{em}, \\ &= \frac{\eta'_Q \cdot H'_{em}}{c_{p, eg} \cdot m_{out}} - T_{em}, \\ &= \frac{\eta'_Q \cdot (H_{out} + \Delta W)}{c_{p, eg} \cdot m_{out}} - T_{em}, \\ &= \frac{\eta'_Q \cdot \left( \frac{H_{em}}{\eta_Q} + \Delta W \right)}{c_{p, eg} \cdot m_{out}} - T_{em}, \\ &= \frac{\eta'_Q - \eta_Q}{\eta_Q} \cdot T_{em} + \frac{\eta'_Q}{c_{p, eg} \cdot m_{out}} \cdot \Delta W.\end{aligned}\quad (43)$$

If  $\eta'_Q \approx \eta_Q$ , we obtain

$$\begin{aligned}\Delta T &\approx \frac{\eta_Q}{c_{p, eg} \cdot m_{out}} \cdot \Delta W, \\ \Rightarrow H'_{em} &= H_{em} + \eta_Q \cdot \Delta W.\end{aligned}\quad (44)$$

Once we know  $\eta_Q$  and  $\Delta W$ , we are able to calculate the temperature increase  $\Delta T$  and the new enthalpy flow  $H'_{em}$ .

### Cylinder deactivation

The deactivation of a cylinder is defined as an operation with closed valves. The deactivated cylinder is assumed to be a perfect gas spring without any additional losses, as shown in Refs.<sup>44,45</sup> In addition, we assume no boost pressure from the turbocharger during cylinder deactivation. The torque generation is described by

$$p_{me} = \frac{n_{act}}{n_{cyl}} \cdot (e \cdot p_{m\phi} + p_{me0g}) + p_{me0f}, \quad (45)$$

where  $n_{act}$  represents the number of cylinders fired. If  $n_{act} = n_{cyl}$ , we recover the previously formulated Willans approximation. In the case of an equal load  $p_{me}$  with  $n_{act} < n_{cyl}$ , the value  $p_{m\phi}$  of the active cylinders has to be increased. As demonstrated above, we assume engine-out quantities to be described by the initial states  $x_{bdc}$  and injection inputs  $u$  of a single cylinder. Therefore, the outputs of a single cylinder such as

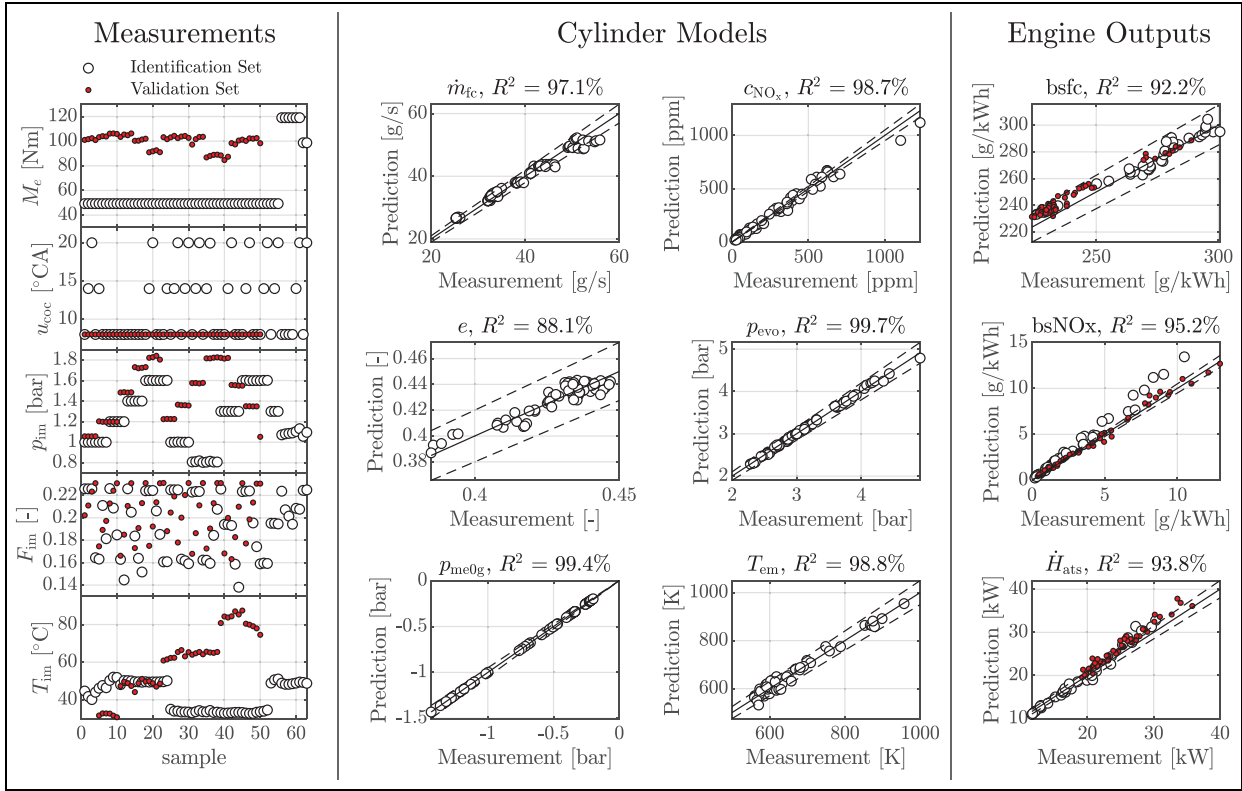


**Figure 14.** Identified models for the engine A at 2000 rpm. The left column of plots show the measurements used for identification and validation. The middle plots show the identified cylinder models. The right column of plots show the results of the complete model including the air path. In all the plots, the dashed lines denote an error margin of 5%.

NOx emissions  $c_{NO_x}$  and engine-out temperature  $T_{em}$  do not change. However, in the case of a cylinder deactivation, we replace  $n_{cyl}$  by  $n_{act}$  and obtain the following mass flows:

$$\begin{aligned} \dot{m}_\varphi &= m_\varphi \cdot \frac{\omega_e \cdot n_{act}}{4 \cdot \pi}, \\ \dot{m}_{fc} &= m_{fc} \cdot \frac{\omega_e \cdot n_{act}}{4 \cdot \pi}, \\ \dot{m}_{out} &= m_{out} \cdot \frac{\omega_e \cdot n_{act}}{4 \cdot \pi}. \end{aligned} \quad (46)$$

The deactivation thus changes the mass flow of NOx and the enthalpy flow to the aftertreatment system, as follows:

$$\begin{aligned} \dot{m}_{ats} &= \dot{m}_{out} - \dot{m}_{lpggr}, \\ \dot{H}_{ats} &\propto \dot{m}_{ats} \cdot T_{em}, \\ \dot{m}_{NO_x} &\propto \dot{m}_{ats} \cdot c_{NO_x}. \end{aligned} \quad (47)$$

## Model identification and validation

In this section, we analyze the models proposed in Section 3. First, we use measurement data obtained from engine A to demonstrate the validity of the proposed cylinder model. We then integrate the cylinder model into an existing air path model to validate the quantities of interest, namely  $\dot{m}_\varphi$ ,  $\dot{m}_{NO_x}$ , and  $\dot{H}_{ats}$ . Measurements obtained from engine B are used to validate the model extensions for the proposed VVT

strategies. The below derived parameters are all listed in Appendix A.5.

## Engine model

The cylinder model derived in Section 3 is based on functions and constants that need to be experimentally identified. Using regression analysis, we propose the following models:

$$\begin{aligned} f_{p_{evo}} &= C_{p_{evo}}^0 + C_{p_{evo}}^1 \cdot m_{ivc} + C_{p_{evo}}^2 \cdot m_\varphi + \dots \\ &\quad C_{p_{evo}}^3 \cdot T_{bdc} + C_{p_{evo}}^4 \cdot u_{coc}, \\ f_e &= C_e^0 + C_e^1 \cdot \Phi + C_e^2 \cdot T_{bdc} + \dots \\ &\quad C_e^3 \cdot u_{coc} + C_e^4 \cdot u_{coc}^2, \\ f_{p_{me0g}} &= C_{p_{me0g}}^1 \cdot \Delta p_{eng} + C_{p_{me0g}}^2 \cdot \Delta p_{eng}^2, \\ f_{c_{NO_x}} &= \exp(C_{c_{NO_x}}^0 + C_{c_{NO_x}}^1 \cdot \Phi + C_{c_{NO_x}}^2 \cdot T_{bdc} + \dots \\ &\quad C_{c_{NO_x}}^3 \cdot F_{ivc} + C_{c_{NO_x}}^4 \cdot u_{coc}), \\ f_{T_{em,ref}} &= C_{T_{em,ref}}^0 + C_{T_{em,ref}}^1 \cdot p_{evo} + C_{T_{em,ref}}^2 \cdot T_{evo}, \end{aligned} \quad (48)$$

where  $C^i$  represents the  $i$ -th constant to be identified. The models mostly consist of linear terms. The left plots of Figure 14 show the data obtained from measurements used for identification and validation of the cylinder models. The results obtained are shown in the middle plots of Figure 14. The cylinder model is then

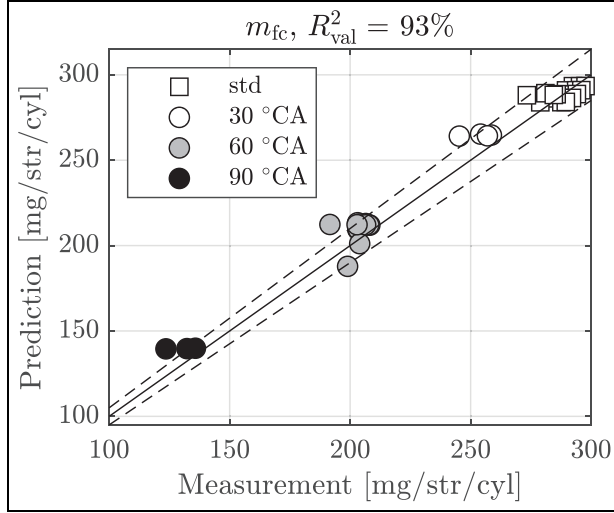


**Figure 15.** Data of engine B. Validation of the reduced cylinder fresh charge  $m_{fc}$  due to various  $\Delta u_{ivc}$ . Measurements with “□” denote the identification set, “○” denote the validation set. The dashed lines denote a 5% error bound.

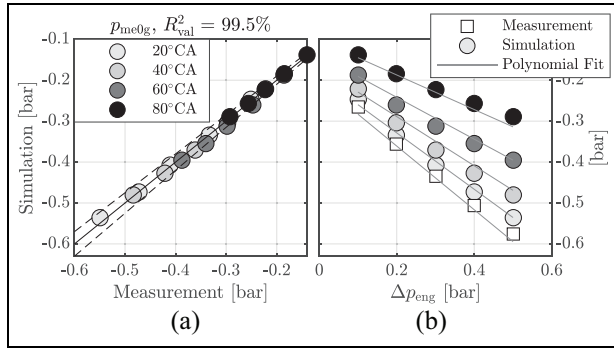


**Figure 16.** Data of engine B. Plot (a) compares the simulation of  $p_{me0g}$  using the presented method compared to measurements, whereas the dashed lines denote a 5% error bound. The legend shows various  $\Delta u_{ivc}$ . Plot (b) shows a polynomial fit of the measurements with standard IVC and simulations.

combined with the air path model in order to simulate the complete engine. The right column of plots of Figure 14 show the steady-state results of engine A for the outputs of interest. We use brake-specific quantities to highlight the effects on the engine outputs: namely the brake-specific fuel consumption bsfc and the brake-specific NOx emissions bsNOx. From the identification and validation data we conclude that the presented model is valid for a wide variety of intake manifold conditions and loads. All parameters identified are listed in Table A2.

### Miller cycle

The three effects of early IVC, which are highlighted in Table 1 and in Section 3.3.1, are validated with measurements from the engine B. First, we validate the

proposed model for the fresh charge. For the identification of the model, we only use measurements with standard IVC, that is, at BDC. Using the model identified, we predict the reduced fresh charge. Figure 15 shows the results. As expected, the fresh charge is reduced proportionally to the reduced displacement volume due to early IVC. Second, we validate the proposed approach to obtain a prediction for the reduced pumping loss  $p_{me0g}$ . Again, only measurements with standard IVC are available for identification. With the method proposed in Section 3.3.1, we simulate the reduced pumping work  $p_{me0g}$  due to early IVC and use the data obtained by simulation to fit a regression model. Plot (a) of Figure 16 shows the simulation results, compared to test-bench measurements. As highlighted in Figure 10, the pumping work is reduced by early IVC. Plot (b) of Figure 16 shows a polynomial fit for the simulated pumping loss of the form

$$\begin{aligned} f_{p_{me0g}} = & C_{p_{me0g}}^1 \cdot \Delta p_{eng} + C_{p_{me0g}}^2 \cdot u_{ivc} + \dots \\ & C_{p_{me0g}}^3 \cdot \Delta p_{eng} \cdot u_{ivc} + \dots \\ & C_{p_{me0g}}^4 \cdot \Delta p_{eng}^2 + C_{p_{me0g}}^5 \cdot u_{ivc}^2. \end{aligned} \quad (49)$$

Finally, the reduced effective compression ratio  $\varepsilon_{eff}$  lowers the cylinder charge temperature  $T_{bdc}$  which affects the outputs thermal efficiency  $e$ , cylinder-out temperature  $T_{em}$ , and engine-out NOx emissions  $c_{NOx}$ . To validate this assumption, we create a measurement grid of various intake manifold conditions  $p_{im}$  and  $T_{im}$  using only standard IVC. The grid variations in intake manifold quantities translate to variations in  $m_{ivc}$  and  $T_{bdc}$  and hence  $x_{bdc}$ . Figure 17 shows the resulting variation in  $x_{bdc}$  and its effects on  $e$ ,  $T_{em}$ , and  $c_{NOx}$ . Plot (a1) shows the variation in  $x_{bdc}$  and the influence on the thermal efficiency  $e$ . The gray area shows a linear affine fit for  $e$ . The residuals are shown in Plot (a2). By starting with fixed values of  $p_{im}$  and  $T_{im}$  and varying values of  $\Delta u_{ivc}$ , the resulting states  $x_{bdc}$  fall into the spanned measurement grid. As plots (a1) and (a2) show, the resulting change in efficiency  $e$ , which is caused by  $\Delta u_{ivc}$ , is well described by a change  $x_{bdc}$ . As pointed out in Section 3.3.1, early IVC leads to a reduction in cylinder mass and an artificial cooling of the cylinder charge. Plots (b1) and (b2) of Figure 17 validate the same effect for the exhaust manifold temperature  $T_{em}$ , whereas plots (c1) and (c2) highlight engine-out NOx emissions. We conclude that the effects of varying the effective compression ratio  $\varepsilon_{eff}$  can be modeled by a variation in  $x_{bdc}$ .

### Early EVO

Since no measurements with early EVO are available for the engine A, we must rely on simulations of the cylinder pressure  $p_{cyl}$  to accurately predict  $\Delta W$ . Using the crank-angle-resolved model, which can be identified with the standard EVO only, we can simulate the work loss  $\Delta W$  presented in equation (36) for various EVO.

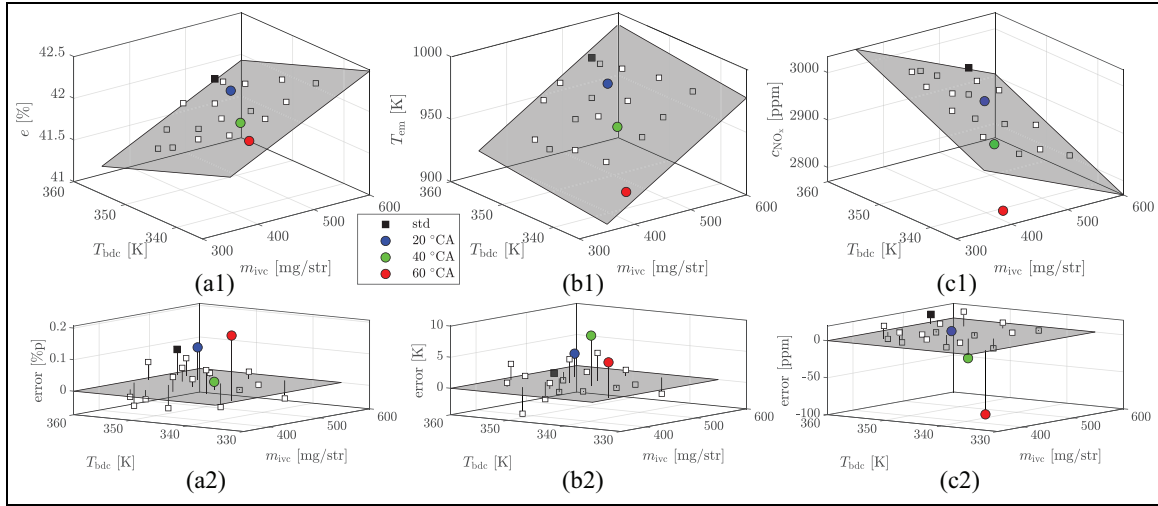


**Figure 17.** Data of engine B. The top plots show the outputs efficiency  $e$ , engine-out temperature  $T_{em}$ , and NOx emissions  $c_{NO_x}$  in relation to the cylinder states at  $x_{bdc}$ . The gridded measurements with standard IVC are denoted as “□”, the measurements “○” denote a variation in  $\Delta u_{ivc}$  as shown in the legend. The gray surfaces are linear fits based on the gridded measurements. The bottom stem plots show the resulting error to a linear fit using standard IVC only. Plots (a1), (b1), and (c1) show the absolute values affected by early IVC, whereas Plots (a2), (b2), and (c2) show the absolute errors.

The validity of this approach is demonstrated in Appendix A.6. The crank-angle-resolved model is then used to create a grid of simulations, from which the following polynomial fit is derived

$$f_{\Delta W} = \Delta p_{evo} \cdot (C_{\Delta W}^1 + C_{\Delta W}^2 \cdot p'_{evo} + C_{\Delta W}^3 \cdot p_{em}). \quad (50)$$

The variable  $\Delta p_{evo}$  represents a change in pressure at EVO which arises due to a change in  $\Delta u_{evo}$ . The change can be calculated using a polytropic equation from the standard EVO by

$$\Delta p_{evo} = p_{evo} \cdot \left( \left( \frac{V_{evo}}{V'_{evo}} \right)^{\gamma_{eg}} - 1 \right), \quad (51)$$

where again  $p_{evo}$  is obtained from the fitted cylinder model shown in equation (48). Using the polynomial fit  $f_{\Delta W}$  allows to quantify the effects on the cylinder outputs as shown in Section 3.3.2. Figure 18 shows the validation for the proposed approach to model early EVO. Plot (a1) shows a comparison between the actual measurement data of  $\Delta W$  and the results of the crank-angle-resolved simulation, while Plot (a2) compares the polynomial fit as proposed in equation (50). Using the fitted model  $f_{\Delta W}$ , we can calculate the drop in  $p_{me}$  as well as the increase in  $H_{em}$  due to early EVO. Plots (b1) and (b2) show the prediction of  $p_{me}$  compared to actual measurements, while Plots (c1) and (c2) show the predictions of  $H_{em}$ . While the model presented seems to somewhat overstate the increase in  $H_{em}$ , the model shows the general trend.

### Cylinder deactivation

We demonstrate the validity of the proposed cylinder deactivation model with measurements from the engine

B. For standard stoichiometric operation without boost pressure, the fuel mass per cylinder defines all quantities, namely  $e$ ,  $p_{me0g}$ ,  $p_{me0f}$ ,  $c_{NO_x}$ ,  $T_{em}$ , and  $\dot{m}_{out}$ . For identification, all quantities are fitted by simple linear affine or quadratic models in dependence of  $p_{m\phi}$ . We then use the proposed models to predict the operation with  $n_{act} = 2$ . Figure 19 shows the results of the proposed method. For all engine outputs  $M_e$ ,  $\dot{m}_{NO_x}$ , and  $\dot{H}_{em}$ , a high accuracy is achieved.

### Case study

We have demonstrated that the cylinder model allows for the simulation of various VVT strategies. Since the cylinder model can be identified with standard valve timing only, there is no need to actually install a VVT. Hence, the model approach presented enables a first evaluation of the advantages of a CI engine with a VVT. As an example, we analyze the effects of a VVT installed on engine A and the impact on the Pareto-optimal trade-off curves for both warm-up operation and stay-warm operation at part load for a single engine operating point. To evaluate the effects on the outputs of interest, we use the complete model including the air path. The operating point is defined in Table 2. Figure 20, which can be found at the end of the paper, shows the results for warm-up operation, that is, when  $T_{ats} = 20^\circ\text{C}$ . The left plots show three different projections of the Pareto-optimal curve, whereas the right plots show the corresponding optimal inputs. The top plots show the bsfc-bsNOx trade-off, which is independent of  $T_{ats}$ . The cylinder deactivation strategy achieves an improvement in bsfc with a slight improvement in bsNOx as indicated by the strategy shift I, whereas early IVC only achieves a slight improvement in bsNOx for similar values of bsfc, as the zoomed-in

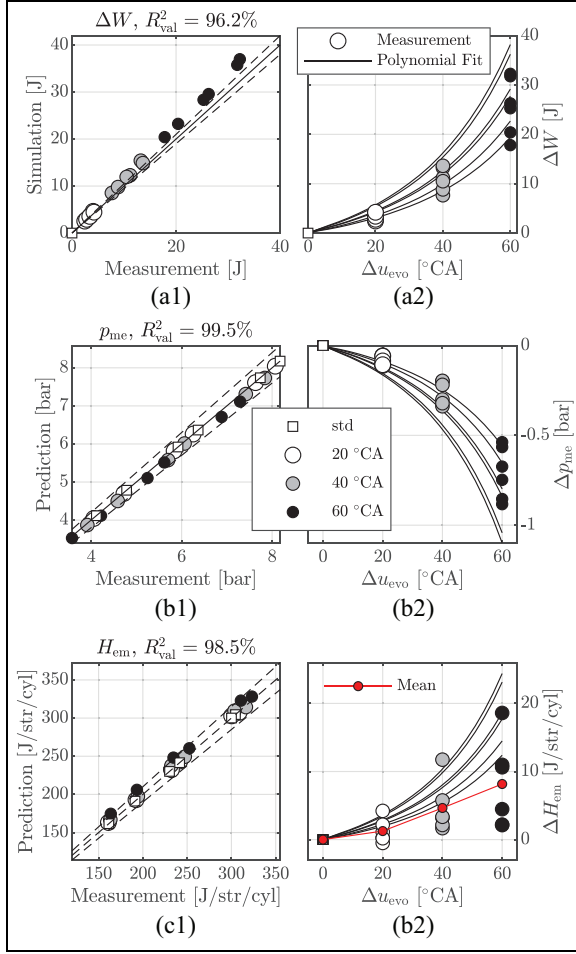


**Figure 18.** Data of engine B. Validation of the work loss  $\Delta W$  due to early EVO for various  $p_{im}$  and  $p_{em}$ . Measurements with “□” denote the identification set; “○” denote the validation set. The legend shows a variation in  $\Delta u_{evo}$ . The dashed lines denote a 5% error margin. The red line in plot (c2) denotes the mean value of all measurements. Plots (a1), (b1), and (c1) show the comparison between prediction and measurement, whereas Plots (a2), (b2), and (c2) show the same results in dependence of early EVO.

plot shows. At the same time, bsfc is improved for the same level of bsNOx. Early EVO is not used as it has no effect in this trade-off. The middle plots show the bsfc- $\dot{H}_{ats}$  trade-off (To maximize  $\dot{H}_{ats}$ , the reciprocal value  $1/\dot{H}_{ats}$  is minimized.). The cylinder deactivation does not show any large improvement in the overall trade-off, whereas a combination of early IVC and early EVO increases  $\dot{H}_{ats}$  without sacrificing bsfc. This effect is due to the fact that variable valve timing increases  $\dot{H}_{ats}$  by mainly increasing  $T_{em}$ , whereas the standard strategy increases  $\dot{H}_{ats}$  by increasing  $\dot{m}_{ats}$ . Without EGR, a high value of  $\dot{m}_{ats}$  is achieved by increasing the boost pressure, which results in increased pumping losses. This results in a significantly higher bsfc for the same level of  $\dot{H}_{ats}$  when compared to a variable valve timing strategy. The bottom plots show the clear advantage of variable valve timing. At cold-start, where the ATS needs to be heated quickly and NOx emissions should be avoided, variable valve timing

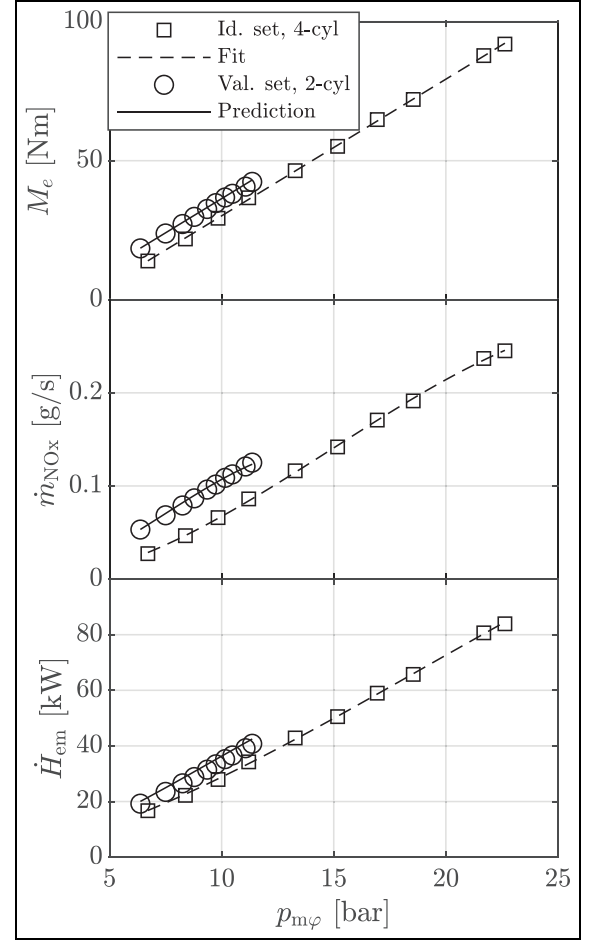


**Figure 19.** Data of engine B. Validation of the proposed cylinder deactivation model. The markers denote measurements, whereas lines denote the predictions of the fitted model. The identification set consists of measurements with all 4 cylinders active, while the validation set consists of engine an operation with only 2 active cylinders.

**Table 2.** The operating point for the case study of engine A.

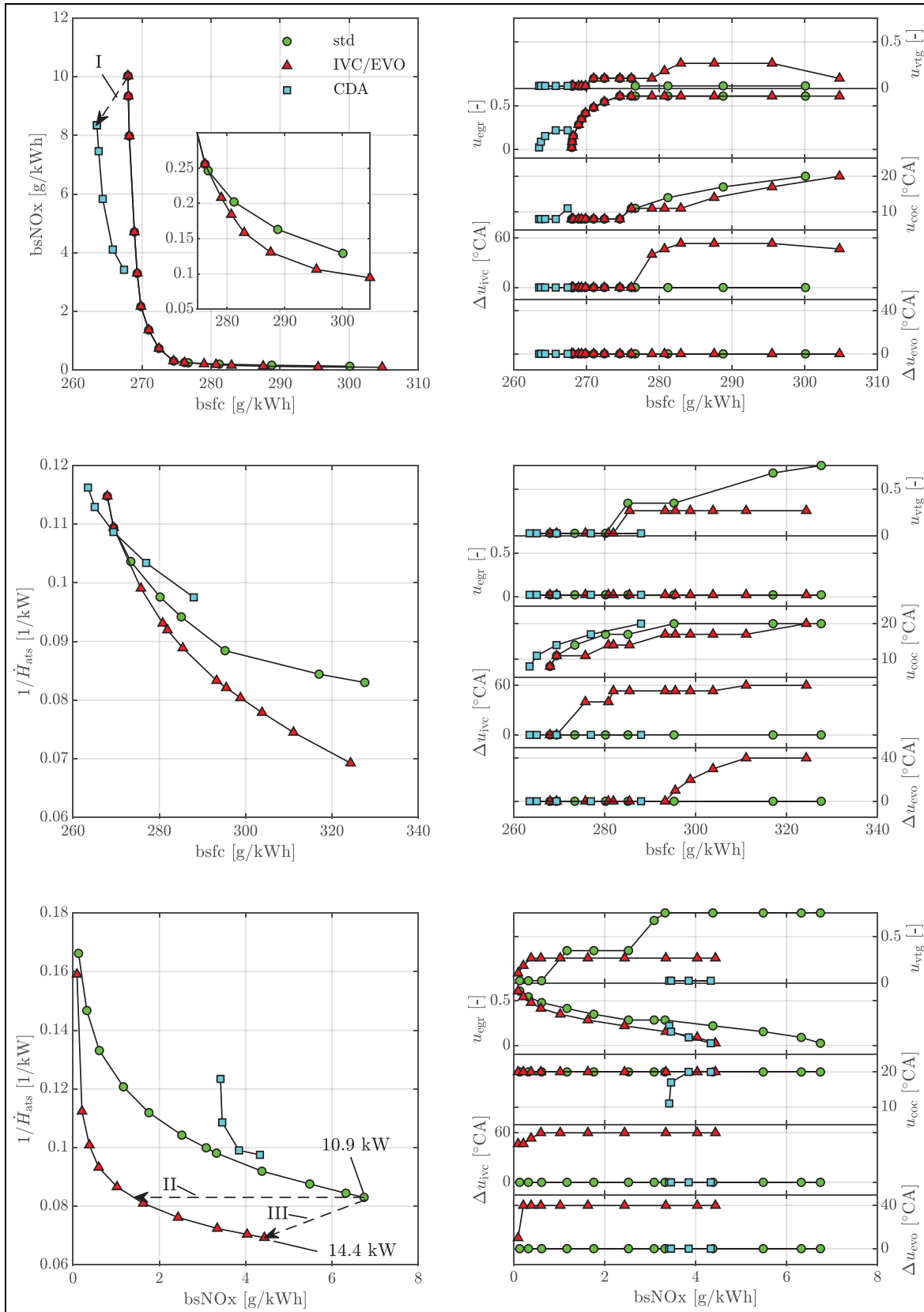
$M_e$	$N_e$	$\Phi_{max}$	$p_{rail}$
50 Nm	2000 rpm	1/1.3	1150 bar

$\Phi_{max}$  represents the smoke limit.

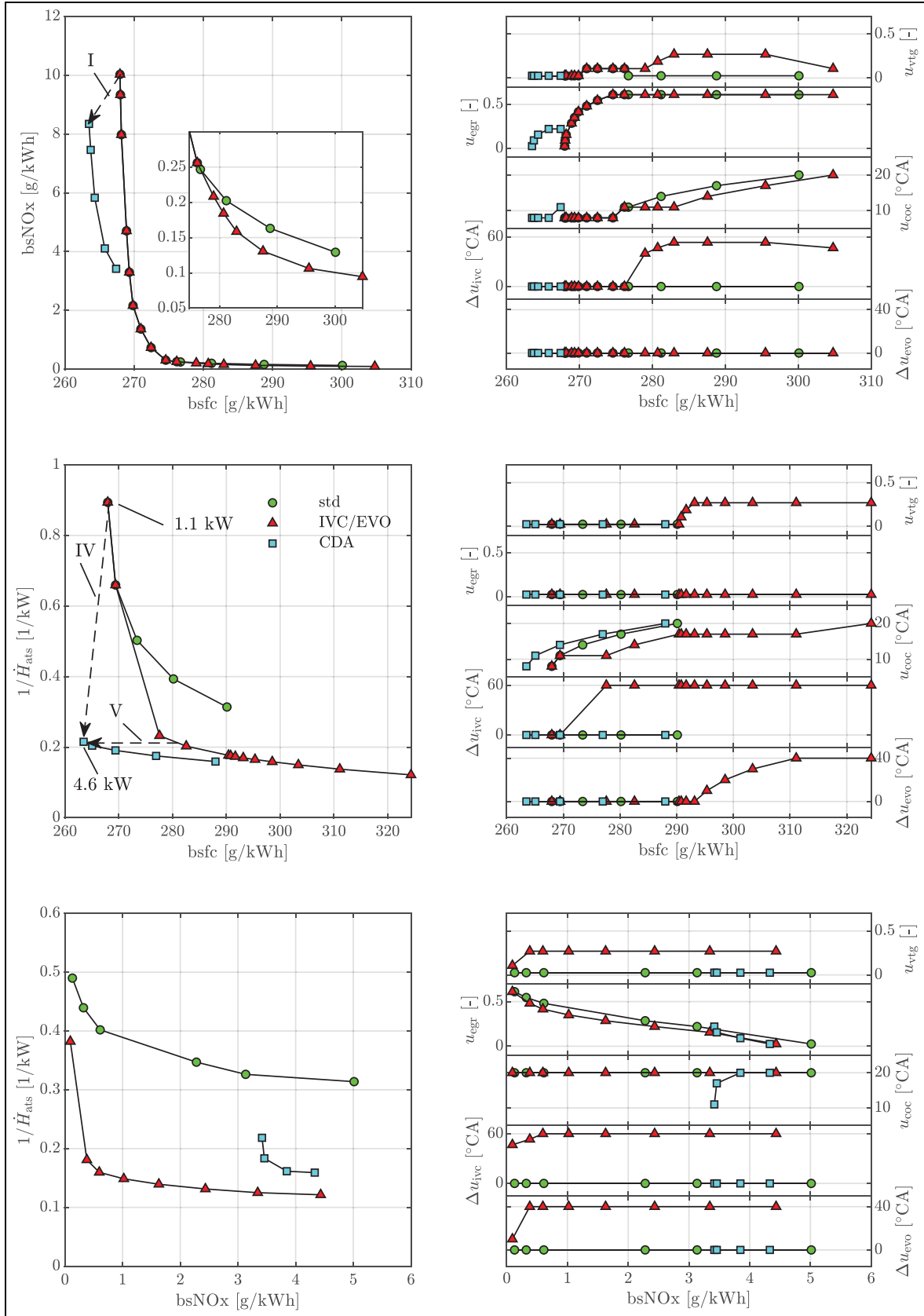
achieves significantly higher levels of  $\dot{H}_{ats}$  while also lowering bsNOx. Two strategy shifts are indicated that might be used with variable valve timing compared to the standard engine layout. Strategy II significantly lowers bsNOx while keeping  $\dot{H}_{ats}$  at roughly 10.9kW, whereas strategy shift III further increases  $\dot{H}_{ats}$  to 14.9kW while also lowering bsNOx. The effect of cylinder deactivation at cold-start is worse than that of the standard strategy since  $\dot{m}_{ats}$  and therefore  $\dot{H}_{ats}$  are strongly reduced.

Figure 21, which can be found at the end of the paper, shows the results for stay-warm operation, that is, when  $T_{ats} = 250^\circ\text{C}$ . Since the SCR-catalyst is able to reduce engine-out NOx emissions, we try to minimize





**Figure 20.** Pareto-optimal trade-off curves for warm-up operation,  $T_{\text{ats}} = 20^{\circ}\text{C}$ . The strategy “std” denotes the standard engine layout, “IVC/EVO” denotes the engine capable of early IVC and early EVO, and “CDA” denotes cylinder deactivation without variable valve timing. The strategy “CDA” uses only two active cylinders and no boost pressure.



**Figure 21.** Pareto-optimal trade-off curves for stay-warm operation,  $T_{ats} = 250^\circ\text{C}$ . The trade-off between bsfc and bsNOx has been omitted since it is not affected by  $T_{ats}$ .

bsfc while also maximizing  $\dot{H}_{\text{ats}}$  to prevent the ATS from further cooling. The advantage of variable valve timing compared to the standard engine layout is also apparent as in warm-up operation. However, cylinder deactivation shows a clear improvement compared to variable valve timing strategies. The top plots of Figure 21 show the bsfc- $\dot{H}_{\text{ats}}$  trade-off. Cylinder deactivation achieves a significant improvement in both bsfc and  $\dot{H}_{\text{ats}}$ . Two possible strategy shifts are indicated. Strategy IV significantly increases  $\dot{H}_{\text{ats}}$  from roughly 1.1 kW to 5 kW while also improving on bsfc, whereas strategy shift V achieves a substantial improvement in bsfc of roughly 20 g/kWh for an equal  $\dot{H}_{\text{ats}}$ . By comparing the fuel-optimal inputs for the indicated strategy shift IV and strategy shift I, we conclude that cylinder deactivation simultaneously improves bsfc, bsNOx, and  $\dot{H}_{\text{ats}}$  when compared to the standard fuel-optimal engine strategy.

Both operating modes, that is, warm-up and stay-warm operation, demonstrate the advantage of a VVT for a single load point, either by using variable valve timing or cylinder deactivation. The obtained Pareto-optimal solutions can be used for a variable engine calibration to obtain fuel-optimal solutions that are compliant with respect to pollutant emission limits as presented in recent studies.<sup>14–16</sup> The quantification of the exact benefit of a VVT for a pre-defined transient cycle will require the identification of the presented models for various engine speeds and the inclusion of a dynamic model for the ATS.

## Conclusion

We have presented a cycle-discrete cylinder model for engines with negative valve overlap. The model, which is based on first principles, is identified with measurements of standard valve timing and can simulate the following VVT strategies: early IVC, early EVO, and cylinder deactivation. Embedded into an existing mean-value model of the air path, we are able to quantify the effects of various VVT strategies on fuel consumption, engine-out NOx emissions, and enthalpy to the ATS at engine steady-state. The complete engine model without VVT has been validated on a CI engine. The model extensions, which allow for the simulation of a VVT, have been validated on a SI engine retrofitted with a VVT. The engine model presented enables a first evaluation of the advantages of an existing engine layout without the need to install a VVT. This is highlighted in the case study, which demonstrates how various VVT strategies can improve engine performance for both warm-up operation and stay-warm operation at part load. For both modes, the case study shows that variable valve timing significantly improves on the trade-off between engine-out NOx emissions and exhaust enthalpy flow when compared to the standard engine strategy. For warm-up operation, cylinder deactivation is unfavorable since the overall mass flow and hence the enthalpy flow to the aftertreatment

system are reduced. For stay-warm operation, cylinder deactivation is more favorable than variable valve timing as efficiency is greatly increased for equal levels of exhaust enthalpy flow. In addition, cylinder deactivation achieves lower fuel consumption, lower NOx emissions, and an increased enthalpy flow when compared to the fuel-optimal standard engine strategy.



## Declaration of conflicting interests

The author(s) declared no potential conflicts of interest with respect to the research, authorship, and/or publication of this article.

## Funding

The author(s) disclosed receipt of the following financial support for the research, authorship, and/or publication of this article: The authors gratefully acknowledge the funding by the Swiss National Science Foundation (SNSF) and the contribution of the Research Unit (FOR) 2401 “Optimization Based Multiscale Control for Low-Temperature Combustion Engines” supported by the German Research Foundation (DFG).

## ORCID iDs

Giordano Moretto  <https://orcid.org/0000-0002-4768-904X>  
Severin Hänggi  <https://orcid.org/0000-0001-8250-4189>

## References

1. Parvate-Patil GB, Hong H and Gordon B. Analysis of variable valve timing events and their effects on single cylinder diesel engine. SAE technical paper 2004-01-2965, 2004. DOI: 10.4271/2004-01-2965.
2. Tomoda T, Ogawa T, Ohki H, Kogo T, Nakatani K and Hashimoto E. Improvement of diesel engine performance by variable valve train system. *Int J Engine Res* 2010; 11(5): 331–344.
3. Töpfer G, Troeger A, Himstedt J, et al. Variable valve actuation as an efficient measure for Off-Highway (OHV) drive systems. In: Liebl J, Beidl C and Maus W (eds) *Internationaler Motorenkongress*. Wiesbaden: Springer Vieweg, 2020, pp.143–157.
4. Hu H, Israel MA and Vorih JM. Variable valve actuation and diesel engine retarding performance. *SAE Trans* 1997; 106: 498–504.
5. Stebler H, Weisser G, Hörler HU and Boulouchos K. Reduction of NOx emissions of D. I. diesel engines by application of the miller-system: an experimental and numerical investigation. *SAE Trans* 1996; 105: 1238–1248.
6. Garg A, Magee M, Ding C, et al. Fuel-efficient exhaust thermal management using cylinder throttling via intake valve closing timing modulation. *Proc IMechE, Part D: J Automobile Engineering* 2016; 230(4): 470–478.
7. Ramesh AK, Shaver GM, Allen CM, et al. Utilizing low airflow strategies, including cylinder deactivation, to improve fuel efficiency and aftertreatment thermal management. *Int J Engine Res* 2017; 18(10): 1005–1016.
8. McCarthy J, Theissl H and Walter L. Improving commercial vehicle emissions and fuel economy with engine temperature management using variable valve actuation.

- In: Liebl J and Beidl C (eds) *Internationaler Motorenkongress*. Wiesbaden: Springer Vieweg, 2017, pp.591–618.
9. Theißl H, Kraxner T, Seitz HF and Kislinger P. Miller-Steuerzeiten für zukünftige nutzfahrzeug-dieselmotoren. *MTZ - Motortechnische Zeitschrift* 2015; 76(11): 18–25.
  10. Horvath A, Seitz HF, Gelter J and Raser B. The future heavy-duty engine - basic engine concept for maximum CO<sub>2</sub> reduction. *MTZ Worldw* 2020; 81(10): 68–72.
  11. Schutting E, Neureiter A, Fuchs C, et al. Miller- und Atkinson-Zyklus am aufgeladenen dieselmotor. *MTZ - Motortechnische Zeitschrift* 2007; 68(6): 480–485.
  12. Guzzella L and Onder CH. *Introduction to modeling and control of internal combustion engine systems*. Berlin, Heidelberg: Springer, 2010.
  13. Elbert P, Amstutz A and Onder C. Adaptive control for the real driving emissions of diesel engines. *MTZ - Motortechnische Zeitschrift* 2017; 78: 76–83.
  14. van Dooren S, Amstutz A and Onder CH. A causal supervisory control strategy for optimal control of a heavy-duty diesel engine with SCR aftertreatment. *Control Eng Pract* 2022; 119: 104982.
  15. Ritzmann J, Chinellato O, Hutter R and Onder C. Optimal integrated emission management through variable engine calibration. *Energies* 2021; 14: 7606.
  16. Ritzmann J, Peterhans C, Chinellato O, Gehlen M and Onder C. Model predictive supervisory control for integrated emission management of diesel engines. *Energies* 2022; 15(8): 2755.
  17. Gehrke S, Kovács D, Eilts P, Rempel A and Eckert P. Investigation of VVA-Based exhaust management strategies by means of a HD single cylinder research engine and rapid prototyping systems. *SAE Int J Commer Veh* 2013; 6(1): 47–61.
  18. Roberts L, Magee M, Shaver G, et al. Modeling the impact of early exhaust valve opening on exhaust aftertreatment thermal management and efficiency for compression ignition engines *Int J Engine Res* 2015; 16(6): 773–794.
  19. Arnau FJ, Martín J, Pla B and Auñón Á. Diesel engine optimization and exhaust thermal management by means of variable valve train strategies. *Int J Engine Res* 2021; 22(4): 1196–1213.
  20. Elicker M, Christgen W, Kiyanni J and Brauer M. Variables ventiltriebkonzept zur Erfüllung zukünftiger emissionsstandards von Dieselfahrzeugen. *MTZ - Motortechnische Zeitschrift* 2021; 82(2): 38–44.
  21. Joshi MC, Gosala D, Shaver GM, McCarthy J and Farrell L. Exhaust valve profile modulation for improved diesel engine curb idle aftertreatment thermal management. *Int J Engine Res* 2021; 22(10): 3179–3195.
  22. Maniatis P, Wagner U and Koch T. A model-based and experimental approach for the determination of suitable variable valve timings for cold start in partial load operation of a passenger car single-cylinder diesel engine. *Int J Engine Res* 2019; 20(1): 141–154.
  23. Maniatis P, Erforth D, Wagner U, et al. Development of valve train configurations optimized for cold start and their effect on diesel soot emission. SAE technical papers 2019-24-0161, 2019. SAE International. DOI: 10.4271/2019-24-0161.
  24. Joshi M, Gosala D, Allen C, et al. Diesel engine cylinder deactivation for improved system performance over transient real-world drive cycles. SAE technical paper 2018-01-0880, 2018. DOI:10.4271/2018-01-0880.
  25. Gosala DB, Ramesh AK, Allen CM, et al. Diesel engine aftertreatment warm-up through early exhaust valve opening and internal exhaust gas recirculation during idle operation. *Int J Engine Res* 2018; 19(7): 758–773.
  26. Gosala DB, Shaver GM, McCarthy JE and Lutz TP. Fuel-efficient thermal management in diesel engines via valvetrain-enabled cylinder ventilation strategies *Int J Engine Res* 2021; 22: 430–442.
  27. Allen CM, Gosala DB, Shaver GM and McCarthy J. Comparative study of diesel engine cylinder deactivation transition strategies. *Int J Engine Res* 2019; 20(5): 570–580.
  28. Allen CM, Joshi MC, Gosala DB, Shaver GM, Farrell L and McCarthy J. Experimental assessment of diesel engine cylinder deactivation performance during low-load transient operations. *Int J Engine Res* 2021; 22: 606–615.
  29. Borgqvist P, Tunestal P and Johansson B. Comparison of negative valve overlap (NVO) and rebreathing valve strategies on a gasoline PPC engine at low load and idle operating conditions. *SAE Int J Engines* 2013; 6(1): 366–378.
  30. Sellnau M, Hoyer K, Moore W, et al. Advancement of GDCI engine technology for US 2025 CAFE and tier 3 emissions. SAE technical paper 2018-01-0901, 2018, pp.1–16. DOI: 10.4271/2018-01-0901
  31. Nevin RM, Sun Y, Gonzalez DMA, et al. PCCI investigation using variable intake valve closing in a heavy duty diesel engine. SAE technical paper 2007-01-0903, 2007, pp.776–790. DOI: 10.4271/2007-01-0903.
  32. Murata Y, Kusaka J, Daisho Y, et al. Miller-PCCI combustion in an HSDI diesel engine with VVT. *SAE Int J Engines* 2008; 1(1): 444–456.
  33. Deng J and Stobart R. BSFC investigation using variable valve timing in a heavy duty diesel engine. SAE technical paper 2009-01-1525, 2009. SAE International. DOI:10.4271/2009-01-1525.
  34. Jia M, Xie M, Wang T and Peng Z. The effect of injection timing and intake valve close timing on performance and emissions of diesel PCCI engine with a full engine cycle CFD simulation. *Appl Energy* 2011; 88(9): 2967–2975.
  35. Hanson RM, Kokjohn SL, Splitter DA and Reitz RD. An experimental investigation of fuel reactivity controlled PCCI combustion in a heavy-duty engine. *SAE Int J Engines* 2010; 3(1): 700–716.
  36. Kokjohn SL, Hanson RM, Splitter DA and Reitz RD. Experiments and modeling of dual-fuel HCCI and PCCI combustion using in-cylinder fuel blending. *SAE Int J Engines* 2009; 2(2): 24–39.
  37. Molina S, García A, Pastor JM, Belarte E and Balloul I. Operating range extension of RCCI combustion concept from low to full load in a heavy-duty engine. *Appl Energy* 2015; 143: 211–227.
  38. Molina S, García A, Monsalve-Serrano J and Estepa D. Miller cycle for improved efficiency, load range and emissions in a heavy-duty engine running under reactivity controlled compression ignition combustion *Appl Therm Eng* 2018; 136: 161–168.
  39. Hänggi S, Frey J, van Dooren S, Diehl M and Onder CH. A modular approach for diesel engine air path control based on nonlinear MPC. *IEEE Trans Control Syst Technol* 2023; 31(4): 1521–1536.

40. Zsiga N, Omanovic A, Soltic P and Schneider W. Functionality and potential of a new electrohydraulic valve train. *MTZ Worldw* 2019; 80(9): 18–27.
41. Heywood JB. *Internal combustion engine fundamentals*. New York: McGraw-Hill Education, 1988. Vol. 21.
42. Moretto G, Hänggi S and Onder C. Optimal combustion calibration for direct-injection compression-ignition engines using multiple injections. *Int J Engine Res* 2023; 24: 1414–1431.
43. Maurya RK. *Reciprocating engine combustion diagnostics*. Cham: Springer, 2019.
44. Ritzmann J, Zsiga N, Peterhans C and Onder C. A control strategy for cylinder deactivation. *Control Eng Pract* 2020; 103: 104566.
45. Zsiga N, Ritzmann J and Soltic P. Practical aspects of cylinder deactivation and reactivation. *Energies* 2021; 14(9): 2540–2620.

## A Appendix

### A.1 Notation

$A_{\text{eff}}$	Effective Valve Area
$p_{\text{me}}$	Brake Mean Effective Pressure
bsfc	Brake Specific Fuel Consumption
bsNO <sub>x</sub>	Brake Specific NO <sub>x</sub> Emissions
$C_j^i$	$i$ – thModel Constant of Variable $j$
$e$	Thermodynamic Efficiency
$N_e$	Engine Speed
$F_{\text{air}}$	Ambient Oxygen Mass Fraction
$p_{\text{m}\phi}$	Fuel Mean Effective Pressure
$p_{\text{me}0}$	Friction Mean Effective Pressure
$p_{\text{me}0f}$	Friction Loss
$p_{\text{me}0g}$	Pumping Loss
$F_{\text{out}}$	Cylinder-out Oxygen Mass Fraction
$\dot{H}_{\text{ats}}$	Enthalpy Flow to ATS
$\dot{H}_{\text{em}}$	Enthalpy Flow into Exhaust Manifold
$\dot{H}_{\text{ev}}$	Crank-angle-resolved Cylinder-out Enthalpy Flow
$\dot{H}_{\text{out}}$	Cylinder-out Enthalpy Flow
$h_{\text{lhv}}$	Lower Heating Value
$\dot{m}_{\text{ats}}$	Exhaust Gas Mass Flow
$\dot{m}_{\text{ev}}$	Crank-angle-resolved Cylinder-out Mass Flow
$\dot{m}_{\text{fc}}$	Aspirated Fresh Charge Mass Flow
$\dot{m}_{\phi}$	Fuel Mass Flow
$\dot{m}_{\text{lpgr}}$	LP EGR Mass Flow
$\dot{m}_{\text{NO}_x}$	NO <sub>x</sub> Mass Flow
$\dot{m}_{\text{out}}$	Cylinder-out Mass Flow
$\dot{m}_{\text{t}}$	Turbine Mass Flow
$n_{\text{cyl}}$	Number of Cylinders
$n_{\text{act}}$	Number of Active Cylinders
$c_{\text{NO}_x}$	NO <sub>x</sub> Concentration
$p_{\text{cr}}$	Critical Pressure
$p_{\text{cyl}}$	Crank-angle-resolved Cylinder Pressure
$p_{\text{em}}$	Exhaust Manifold Pressure
$p_{\text{im}}$	Intake Manifold Pressure
$p_{\text{rail}}$	Rail Pressure
$p_{\text{ref}}$	Reference Pressure

$\dot{Q}_{\text{loss}}$	Heat Loss Exhaust Piping
$R_{\text{air}}$	Ideal Gas Constant, Air
$R_{\text{eg}}$	Ideal Gas Constant, Exhaust Gas
$R^2$	Coefficient of Determination, Id. Set
$R_{\text{val}}^2$	Coefficient of Determination, Val. Set
$T_{\text{at}}$	Temperature after Turbine
$T_{\text{ats}}$	ATS Temperature
$T_{\text{cyl}}$	Crank-angle-resolved Cylinder Temperature
$T_{\text{em,ref}}$	Temperature at Reference Pressure
$M_e$	Engine Torque
$T_{\text{out}}$	Cylinder-out Mean Temperature
$u_{\text{coc}}$	Center of Combustion
$V_c$	Cylinder Clearance Volume
$V_d$	Cylinder Displacement Volume
$u$	Standard Cylinder Inputs
$u_{\text{vvt}}$	VVT Cylinder Inputs
$x$	Cylinder States
$W_{\text{hp}}$	High-Pressure Indicated Work
$W_{\text{lp}}$	Low-Pressure Indicated Work
$W_{\text{lp, sim}}$	Simulated Low-Pressure Indicated Work
$c_p$	Specific Heat at Constant Pressure
$c_v$	Specific Heat at Constant Volume
$F$	Oxygen Mass Fraction
$f_j$	Model Fit for Variable $j$
$m$	Cylinder Mass
$s$	Entropy
$V$	Cylinder Volume
$v$	Specific Volume
$X$	Residual Gas Mass Fraction

### Greek symbols

$\Delta p_{\text{eng}}$	Pressure Difference over Engine
$\Delta p_{\text{evo}}$	Change in EVO Pressure due to Early EVO
$\Delta T$	Increase in Exhaust Temperature due to Early EVO
$\Delta u_{\text{evo}}$	Change from standard EVO
$\Delta u_{\text{ivc}}$	Change from standard IVC
$\Delta W$	Loss of Work due to Early EVO
$\varepsilon_{\text{eff}}$	Effective Compression Ratio
$\eta_Q$	Heat Transfer Efficiency
$\gamma_{\text{air}}$	Polytropic Coefficient, Air
$\gamma_{\text{eg}}$	Polytropic Coefficient, Exhaust Gas
$\omega_e$	Engine Angular Velocity
$\Phi$	Fuel-to-Air Ratio
$\Phi_{\text{max}}$	Smoke Limit
$\Psi$	Flow Function
$\sigma_0$	Stoichiometric Coefficient for Air
$\sigma_{\text{O}_2}$	Stoichiometric Coefficient for Oxygen
$\theta$	Crank Angle
$\lambda_1$	Volumetric Efficiency

### Acronyms

ATS	Aftertreatment System
BDC	Bottom Dead Center
CDA	Cylinder Deactivation



CFD	Computational Fluid Dynamics
COC	Center of Combustion
EB	Exhaust Brake
EGR	Exhaust Gas Recirculation
EM	Exhaust Manifold
EVC	Exhaust Valve Closing
EVO	Exhaust Valve Opening
FC	Fresh Charge
FPGA	Field Programmable Gate Array
HP	High Pressure
IC	Intercooler
IM	Intake Manifold
IVC	Intake Valve Closing
IVO	Intake Valve Opening
LHV	Lower Heating Value
LP	Low Pressure
NDIR	Nondispersive Infrared
RCP	Rapid Control Prototyping
SCR	Selective Catalytic Reduction
TC	Turbocharger
VTG	Variable Turbine Geometry
VVT	Variable Valve Train

## A.2 Engine specifications

**Table A1.** Specifications of the two engines.

Engine	Engine A (EA189)	Engine B (EA111)
$n_{cyl}$	4	4
$V_d$ [cm <sup>3</sup> ]	492	348
max $M_e$ [Nm]	320	160
max $N_e$ [rpm]	4500	5500
Fuel	Diesel	Natural Gas
Injection	Direct Injection	Port-Fuel Injection
Ignition	Compression Ignition	Spark Ignition

## A.3 Derivations

### Equations (21):

As proposed in literature,<sup>43</sup> the cylinder temperature at IVC is found by assuming adiabatic mixing of the residual gas with the fresh charge gas at a constant volume. Hence, energy conservation reads

$$c_{v,ivc} \cdot m_{ivc} \cdot T_{ivc} = c_{v,air} \cdot m_{fc} \cdot T_{im} + c_{v,eg} \cdot m_{evc} \cdot T_{evc}, \quad (A.1)$$

which can be rearranged as

$$T_{ivc} = \frac{1}{c_{v,ivc}} \cdot \left( c_{v,air} \cdot \frac{m_{fc}}{m_{ivc}} \cdot T_{im} + c_{v,eg} \cdot \frac{m_{evc}}{m_{ivc}} \cdot T_{evc} \right). \quad (A.2)$$

The mass conservation reads

$$m_{ivc} = m_{fc} + m_{evc}. \quad (A.3)$$

Using the residual gas mass fraction  $X_{res}$  of equation (22), we can express the specific heat capacity at IVC by a mass-weighted mean

$$c_{v,ivc} = (1 - X_{evc}) \cdot c_{v,air} + X_{evc} \cdot c_{v,eg}. \quad (A.4)$$

Using the above equations we derive the expression

$$T_{ivc}^k = \frac{(1 - X_{evc}^k) \cdot c_{v,air} \cdot T_{im}^k + X_{evc}^k \cdot c_{v,eg} \cdot T_{evc}^k}{(1 - X_{evc}^k) \cdot c_{v,air} + X_{evc}^k \cdot c_{v,eg}}. \quad (A.5)$$

### Equations (28):

Using the fact that

$$m_{evo}^k = m_{fc}^k + m_{evc}^k + m_{\phi}^k, \quad (A.6)$$

together with the ideal gas equation

$$T_{evo} = \frac{p_{evo} \cdot V_{evo}}{R_{eg} \cdot m_{evo}}, \quad (A.7)$$

Equation (26) reads

$$\begin{aligned} T_{evc}^{k+1} &= T_{evo}^k \cdot \left( \frac{p_{em}^k}{p_{evo}^k} \right)^{\frac{\gamma_{eg}-1}{\gamma_{eg}}}, \\ &= \left( \frac{p_{evo}^k \cdot V_{evo}^k}{(m_{fc}^k + m_{evc}^k + m_{\phi}^k) \cdot R_{eg}} \right) \cdot \left( \frac{p_{em}^k}{p_{evo}^k} \right)^{\frac{\gamma_{eg}-1}{\gamma_{eg}}}. \end{aligned} \quad (A.8)$$

Using the above derived equation and the ideal gas equation at EVC

$$m_{evc}^{k+1} = \frac{p_{evc}^k \cdot V_{evc}^k}{R_{eg} \cdot T_{evc}^k}, \quad (A.9)$$

in addition to the assumption  $p_{evc} = p_{em}$ , yields

$$\begin{aligned} m_{evc}^{k+1} &= \frac{p_{em}^k \cdot V_{evc}^k \cdot (m_{fc}^k + m_{evc}^k + m_{\phi}^k) \cdot R_{eg}}{R_{eg} \cdot p_{evo}^k \cdot V_{evo}^k} \cdot \left( \frac{p_{em}^k}{p_{evo}^k} \right)^{\frac{1-\gamma_{eg}}{\gamma_{eg}}}, \\ &= (m_{fc}^k + m_{evc}^k + m_{\phi}^k) \cdot \left( \frac{V_{evc}^k}{V_{evo}^k} \right) \cdot \left( \frac{p_{em}^k}{p_{evo}^k} \right)^{\frac{1}{\gamma_{eg}}}. \end{aligned} \quad (A.10)$$

## A.4 Control volume “cylinder”

We analyze the control volume “cylinder” on a crank-angle-resolved, zero-dimensional basis. The control volume is an open, adiabatic system with a changing volume due to piston motion. The variable time  $t$  is used as independent variable. Using mass and energy conservation, the following system of ordinary differential equations is derived:

$$\begin{aligned} \frac{d}{dt} p_{\text{cyl}} &= -\frac{\gamma_{\text{eg}}}{V} \cdot p_{\text{cyl}} \cdot \frac{dV}{dt} + \frac{\gamma_{\text{eg}} - 1}{V} \cdot c_{p,\text{eg}} \cdot T_{\text{cyl}} \cdot \dot{m}_{\text{ev}}, \\ \frac{d}{dt} T_{\text{cyl}} &= \frac{T_{\text{cyl}} \cdot R}{p_{\text{cyl}} \cdot V \cdot c_{v,\text{eg}}} \cdot \dots \\ &\quad \left( -p_{\text{cyl}} \cdot \frac{dV}{dt} + (c_{p,\text{eg}} - c_{v,\text{eg}}) \cdot T_{\text{cyl}} \cdot \dot{m}_{\text{ev}} \right), \end{aligned} \quad (\text{A.11})$$

where the mass flow over the exhaust valve is obtained by the isenthalpic throttle equation

$$\dot{m}_{\text{ev}} = \begin{cases} A_{\text{eff}}(t) \cdot \frac{p_{\text{cyl}}}{\sqrt{R \cdot T_{\text{cyl}}}} \cdot \Psi\left(\frac{p_{\text{cyl}}}{p_{\text{em}}}\right), & p_{\text{cyl}} > p_{\text{em}} \\ A_{\text{eff}}(t) \cdot \frac{p_{\text{em}}}{\sqrt{R \cdot T_{\text{cyl}}}} \cdot \Psi\left(\frac{p_{\text{em}}}{p_{\text{cyl}}}\right), & p_{\text{cyl}} < p_{\text{em}} \end{cases} \quad (\text{A.12})$$

with the so-called flow function

$$\Psi\left(\frac{p_{\text{cyl}}}{p_{\text{em}}}\right) = \dots \begin{cases} \sqrt{\gamma_{\text{eg}} \cdot \left(\frac{2}{\gamma_{\text{eg}} + 1}\right)^{\frac{\gamma_{\text{eg}} + 1}{\gamma_{\text{eg}} - 1}}}, & p_{\text{em}} < p_{\text{cr}} \\ \left(\frac{p_{\text{em}}}{p_{\text{cyl}}}\right)^{\frac{1}{\gamma_{\text{eg}}}} \cdot \sqrt{\frac{2 \cdot \gamma_{\text{eg}}}{\gamma_{\text{eg}} - 1} \cdot \left(1 - \left[\frac{p_{\text{em}}}{p_{\text{cyl}}}\right]^{\frac{\gamma_{\text{eg}} - 1}{\gamma_{\text{eg}}}}\right)}, & p_{\text{em}} > p_{\text{cr}} \end{cases} \quad (\text{A.13})$$

and critical pressure

$$p_{\text{cr}} = \left(\frac{2}{\gamma_{\text{eg}} + 1}\right)^{\frac{\gamma_{\text{eg}}}{\gamma_{\text{eg}} - 1}} \cdot p_{\text{cyl}} \quad (\text{A.14})$$

The only parameter for this system is the effective valve area  $A_{\text{eff}}(t)$ , which can be identified using measurements of the cylinder pressure  $p_{\text{cyl}}$ . The shape of  $A_{\text{eff}}$ , as shown in Figure 7, is described by a few parameters. The above stated equations can be abbreviated as

$$\frac{d}{dt} x = f_{\text{cyl}}(x, t, A_{\text{eff}}, p_{\text{em}}), \quad (\text{A.15})$$

where  $x := [p_{\text{cyl}}, T_{\text{cyl}}]^T$  represents the state vector,  $A_{\text{eff}}$  is the valve area identified, and  $p_{\text{em}}$  is the exhaust manifold pressure. Using the above system and the initial conditions  $x_0 := [p_{\text{evo}}, T_{\text{evo}}]^T$ , the instantaneous enthalpy leaving the control volume is defined by

$$\dot{H}_{\text{ev}} = c_{p,\text{eg}} \cdot \dot{m}_{\text{ev}} \cdot T_{\text{cyl}} \quad (\text{A.16})$$

The complete enthalpy  $H_{\text{out}}$  and mass  $m_{\text{out}}$  that leave the cylinder during the discharge process are obtained by integration

$$\begin{aligned} m_{\text{out}} &= \int_{t_{\text{evo}}}^{t_{\text{evc}}} \dot{m}_{\text{ev}} \, dt, \\ H_{\text{out}} &= \int_{t_{\text{evo}}}^{t_{\text{evc}}} \dot{H}_{\text{ev}} \, dt. \end{aligned} \quad (\text{A.17})$$

The mean temperature  $T_{\text{out}}$  is

$$T_{\text{out}} = \frac{\int_{t_{\text{evo}}}^{t_{\text{evc}}} c_{p,\text{eg}} \cdot \dot{m}_{\text{ev}} \cdot T_{\text{cyl}} \, dt}{\int_{t_{\text{evo}}}^{t_{\text{evc}}} c_{p,\text{eg}} \cdot \dot{m}_{\text{ev}} \, dt}, \quad (\text{A.18})$$

which has also been described as the enthalpy-averaged temperature.<sup>41</sup>

## A.5 Parameters

Table A2 lists the parameters for the cylinder model of engine A. Tables A3 and A4 list the parameters for the model extensions of engine A and B, respectively.

**Table A2.** Parameters of standard cylinder model for engine A.

Model	Factor	Parameter	Value
$f_{p_{\text{evo}}}$	I	$C_{p_{\text{evo}}}^0$	$-1.62 \cdot 10^5$
	$m_{\text{IVC}}$	$C_{p_{\text{evo}}}^1$	$2.38 \cdot 10^8$
	$m_{\varphi}$	$C_{p_{\text{evo}}}^2$	$1.26 \cdot 10^{10}$
	$T_{\text{bdc}}$	$C_{p_{\text{evo}}}^3$	349
	$u_{\text{coc}}$	$C_{p_{\text{evo}}}^4$	2070
$f_e$	I	$C_e^0$	$4.65 \cdot 10^{-1}$
	$\Phi$	$C_e^1$	$-4.25 \cdot 10^{-2}$
	$T_{\text{bdc}}$	$C_e^2$	$-6.91 \cdot 10^{-5}$
	$u_{\text{coc}}$	$C_e^3$	$3.40 \cdot 10^{-3}$
	$u_{\text{coc}}^2$	$C_e^4$	$-2.15 \cdot 10^{-4}$
$*f_{\text{cNO}_x}$	I	$C_{\text{cNO}_x}^0$	-4.80
	$\Phi$	$C_{\text{cNO}_x}^1$	1.53
	$T_{\text{bdc}}$	$C_{\text{cNO}_x}^2$	$7.40 \cdot 10^{-3}$
	$F_{\text{IVC}}$	$C_{\text{cNO}_x}^3$	38.6
	$u_{\text{coc}}$	$C_{\text{cNO}_x}^4$	$-6.39 \cdot 10^{-2}$
$f_{T_{\text{em,ref}}}$	I	$C_{T_{\text{em,ref}}}^0$	130
	$p_{\text{evo}}$	$C_{T_{\text{em,ref}}}^1$	$-4.63 \cdot 10^{-4}$
	$T_{\text{evo}}$	$C_{T_{\text{em,ref}}}^2$	$7.38 \cdot 10^{-1}$
Other		$C_{\lambda_1}$	$9.62 \cdot 10^{-1}$
		$C_{T_{\text{IVC}}}$	33.9
		$C_{p_{\text{medf}}}$	$1.06 \cdot 10^5$

## A.6 Identification cylinder model

The effective valve area  $A_{\text{eff}}$  is the only parameter for the crank-angle-resolved cylinder model which was presented in Appendix A.4. The effective valve area  $A_{\text{eff}}$ , which can be identified with standard EVO only, is used to simulate the cylinder pressure for various EVO. The presented approach is validated on the engine B,

**Table A3.** Parameters for VVT model extensions of engine A.

Model	Factor	Parameter	Value
$f_{p_{me0g}}$	$\Delta p_{eng}$	$C_{p_{me0g}}^1$	-1.68
	$u_{ivc}$	$C_{p_{me0g}}^2$	94.3
	$\Delta p_{eng} \cdot u_{ivc}$	$C_{p_{me0g}}^3$	$-2.84 \cdot 10^{-3}$
	$\Delta p_{eng}^2$	$C_{p_{me0g}}^4$	$1.82 \cdot 10^{-6}$
	$u_{ivc}^2$	$C_{p_{me0g}}^5$	$3.06 \cdot 10^{-1}$
$\Delta W$	1	$C_{\Delta W}^1$	$9.92 \cdot 10^{-5}$
	$p'_{evo}$	$C_{\Delta W}^2$	$5.87 \cdot 10^{-11}$
	$p_{em}$	$C_{\Delta W}^3$	$-3.75 \cdot 10^{-10}$

**Table A4.** Parameters for VVT model extensions of engine B.

Model	Factor	Parameter	Value
$f_{p_{me0g}}$	$\Delta p_{eng}$	$C_{p_{me0g}}^1$	-1.82
	$u_{ivc}$	$C_{p_{me0g}}^2$	255
	$\Delta p_{eng} \cdot u_{ivc}$	$C_{p_{me0g}}^3$	$-4.43 \cdot 10^{-3}$
	$\Delta p_{eng}^2$	$C_{p_{me0g}}^4$	$3.79 \cdot 10^{-6}$
	$u_{ivc}^2$	$C_{p_{me0g}}^5$	$8.53 \cdot 10^{-1}$
$\Delta W$	1	$C_{\Delta W}^1$	$8.16 \cdot 10^{-5}$
	$p'_{evo}$	$C_{\Delta W}^2$	$4.84 \cdot 10^{-11}$
	$p_{em}$	$C_{\Delta W}^3$	$-1.37 \cdot 10^{-10}$

where actual measurements of early EVO are available for validation. The cylinder pressure  $p'_{cyl}$  for early EVO is simulated with the initial conditions  $x'_{evo}$ , which are obtained by the polytropic relation

$$p'_{evo} = f_{p_{evo}}(x_{bdc}, \mathbf{u}) \cdot \left( \frac{V_{cyl}}{V'_{evo}} \right)^{\gamma_{eg}}. \quad (A.19)$$

The quantity  $f_{p_{evo}}(\cdot)$  is obtained from measurement data with standard EVO. Figure A1 shows the validation of the proposed approach. Plots (a1) and (a2) show the cylinder pressure for standard EVO and early EVO,

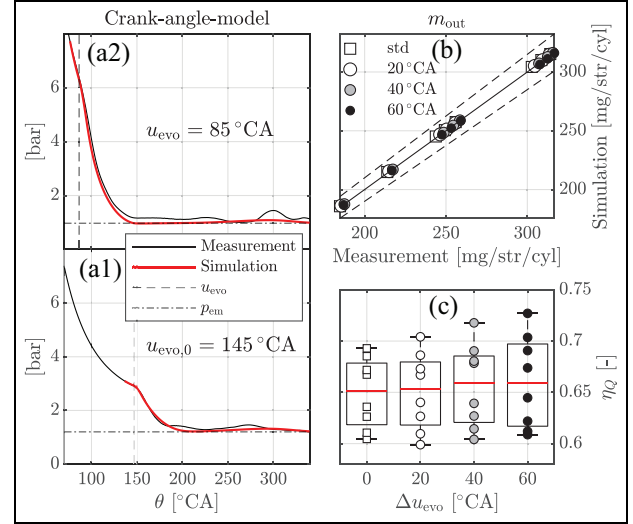


**Figure A1.** Data of engine B. Plots (a1) and (a2) show the cylinder pressure  $p_{cyl}$  of the identified crank-angle-resolved cylinder model. Plot (b) shows the simulated engine-out mass per cycle per cylinder for various  $u_{evo}$  and  $\Delta p_{eng}$  in comparison to measurement data, whereas “□” denotes the identification set and “○” the validation set. The legend denotes the values of increasing  $\Delta u_{evo}$ . The dashed lines denote a 5% error margin. Plot (c) shows the box-plots for the various simulated  $\eta_Q$ . The red line denotes the median value.

respectively. The simulation of  $p_{cyl}$  is in good agreement with the actual measurements for various EVO. In addition, the simulated engine-out mass  $m_{out}$  is also predicted well when compared to actual measurements as Plot (b) of Figure A1 shows. Furthermore, the crank-angle-resolved simulation allows to quantify  $H_{out}$ , which together with the measured enthalpy flow  $H_{em}$  is used to estimate  $\eta_Q$ . As Plot (c) of Figure A1 shows,  $\eta_Q$  is approximately constant. To keep the model simple, a constant  $\eta_Q$  will be used for the prediction of  $H_{em}$  for various EVO.